The small-scale dynamo in the low-Mach number regime

A Thesis

submitted to

Indian Institute of Science Education and Research Pune

in partial fulfillment of the requirements for the

BS-MS Dual Degree Programme

by

Radhika A C

Indian Institute of Science Education and Research Pune

Dr. Homi Bhabha Road,

Pashan, Pune 411008, INDIA.

April, 2020

Supervisor: Prof. Dr. Robi Banerjee and A/Prof. Christoph Federrath

© Radhika A C 2020

Certificate

This is to certify that this dissertation entitled *The small-scale dynamo in the low-Mach number regime* towards the partial fulfilment of the BS-MS dual degree programme at the Indian Institute of Science Education and Research, Pune represents study/work carried out by Radhika A C at the University of Hamburg and the Australian National University under the supervision of Prof. Dr. Robi Banerjee and A/Prof. Christoph Federrath, during the academic year 2019-2020.

Prof. Dr. Robi Banerjee and A/Prof. Christoph Federrath   Radhika A C

Committee:

    Prof. Dr. Robi Banerjee and A/Prof. Christoph Federrath

    Prof. Prasad Subramanian

This thesis is dedicated to

My Grandparents and My Parents
My Brother
&
Neha

Declaration

I hereby declare that the matter embodied in the report entitled *The small-scale dynamo in the low-Mach number regime*, is the result of the work carried out by me at the Department Physics, University of Hamburg and Australian National University, under the supervision of Prof. Dr. Robi Banerjee and A/Prof. Christoph Federrath and the same has not been submitted elsewhere for any other degree.

Prof. Dr. Robi Banerjee and A/Prof. Christoph Federrath   Radhika A C

Acknowledgment

I am deeply indebted to my supervisors, Prof. Robi Banerjee and A/Prof. Christoph Federrath for their guidance and mentorship throughout this project. I am very grateful to the students and staff members of the University of Hamburg and the Australian National University for hosting me during the course of the project. I would also like to thank Dr. Pranjal Trivedi, Postdoctoral Research Fellow, University of Hamburg, for his guidance and insights on this project.

I would like to thank my family for all their love and support. I would further like to express my gratitude and love to all my friends who have cherished me, sustained me and shared this 5 year long journey with me.

x

Abstract

We present the first study on the amplification of magnetic fields by the small-scale turbulent dynamo (SSD) in the highly subsonic regime, with Mach numbers ranging from 10^{-3} to 0.4. We study the properties of the SSD as a function of the nature of turbulent driving, in particular the compressive (curl-free) and the solenoidal (divergence-free) driving. We find that for the lower Mach numbers, the saturation efficiency of the dynamo, $(E_{\mathrm{mag}}/E_{\mathrm{kin}})_{\mathrm{sat}}$, increases as the Mach number decreases. Even in the case when injection of energy is purely through longitudinal forcing modes (or no solenoidal component in the turbulent driving), $(E_{\mathrm{mag}}/E_{\mathrm{kin}})_{\mathrm{sat}} \sim 10^{-2}$ at a Mach number of 10^{-3}. We also find that increasing the solenoidal fraction in the driving field increases the saturation efficiency and the amplification rate of the SSD. We apply our results to magnetic field amplification in the early Universe and predict that a SSD can amplify magnetic fields to $\gtrsim 10^{-16}$ Gauss on scales of 0.1 pc and $\gtrsim 10^{-13}$ Gauss on scales of 100 pc. This result can explain the intergalactic magnetic fields inferred from blazer γ-ray observations on these scales. We also apply our findings on the low Mach number SSD to the solar corona and the hot interstellar medium in the galactic corona.

Contents

Permission

This thesis is based on the following work which has been submitted for publication (currently to the American Physical Society's Physical Review Letters)

- Efficient highly-subsonic turbulent dynamo and growth of primordial magnetic fields, Radhika Achikanath Chirakkara, Christoph Federrath, Pranjal Trivedi and Robi Banerjee

List of Figures

3

List of Tables

Chapter 1

Introduction

Magnetic fields are ubiquitous at all scales in the Universe, from the surface of stars to galaxies to the voids in the large-scale structure of the Universe. Several studies have inferred the presence of intergalactic magnetic fields (IGMFs) through blazar γ-ray observations of TeV blazars and have predicted a lower limit of 10^{-18}–10^{-16} Gauss for the IGMF on Mpc scales [1, 2, 3, 4, 5, 6, 7, 8]. The legitimacy of these observations has been questioned due to the possible effect of plasma instabilities in the intergalactic medium [9]. However, recent studies by [10] and [11], which have taken into account the impact of plasma instabilities on the observations, have shown that a lower bound on the IGMF can be estimated faithfully from the γ-ray observations. The magnetic field strengths estimated from the $\gamma-$ ray observations depend on the correlation length of the magnetic field in consideration. At smaller scales the magnetic field strength increases roughly as square root of the correlation scale [1]. This gives us magnetic fields with strengths $10^{-17} - 10^{-14}$ Gauss on scales of 0.1 pc and field strengths of $10^{-19} - 10^{-15}$ Gauss on 100 pc scales [7, 8].

Understanding the origin of these magnetic fields is an unsolved problem, and the cosmological origin of these magnetic fields have been discussed in previous studies. Magnetic fields can be generated during various phases in the early Universe [12]. [13] predict the generation of magnetic fields with strength $\sim 10^{-29}$ Gauss at the electroweak phase transition and field strengths of $\sim 10^{-20}$ Gauss at the QCD phase transition. [14] predict magnetic fields with strengths $\sim 10^{-34}$–10^{-10} Gauss on a scale of 1 Mpc may be produced during inflation. Otherwise, the unavoidable presence of vorticity in the primordial plasma leads to the generation of weak magnetic fields in the radiation era [15, 16].

The observed magnetic fields, in many cases, are orders of magnitude higher than the initially

generated fields. To explain the magnitude of the observed strong magnetic fields in the voids of the Universe, [17] showed that the small-scale dynamo (SSD) could amplify the magnetic field seeds present in the early Universe. The SSD amplifies small initial seed magnetic fields, by converting turbulent kinetic energy into magnetic energy and causing an exponential amplification of the magnetic field [18, 19, 20]. The SSD has a wide range of applications as it can operate in a variety of astrophysical situations and has been studied in the supersonic and transonic regimes [21, 22].

Velocity fluctuations are required to drive turbulence in the early Universe, which is necessary for the SSD mechanism. The authors of [17] have put forward two mechanisms for generating turbulence in the early Universe: (i) Turbulence from primordial density perturbations and (ii) Turbulence from first-order phase transitions and have shown that all the criteria for the amplification of magnetic fields by the SSD dynamo are met in the early Universe. They have shown that the Reynolds number of the plasma (Re) is very high in the early Universe. The magnetic Reynolds number, Rm, is very high in the early Universe as well, Rm $\sim 10^8 - 10^{12}$. This is sufficiently above the critical value of the Magnetic Reynolds number required for dynamo action [23]. The authors also show that the magnetic Prandtl number (Pm) is very high as well. Analytical and semi-analytical studies in this high Pm regime have been conducted to understand the growth rates and saturation efficiencies of the SSD [23, 24].

Turbulence in the early Universe is unavoidably generated by the gravitational acceleration due to the primordial density fluctuations, which gives rise to longitudinal (irrotational) driving modes primarily. We are, therefore, interested in this case when the dynamo is driven solely by longitudinal velocity modes. From [17], we expect the SSD in the early Universe to have operated under very subsonic conditions with Mach numbers ($\mathcal{M}$) $\sim 10^{-5}$–10^{-4} for a dynamo driven by the primordial density fluctuations. In the case of the dynamo being driven by first-order phase transitions, the Mach numbers can be significantly higher. Motivated by these predictions, we study the behavior of the SSD in the very subsonic regime with a purely compressive (or longitudinal) driving of the turbulence. In addition to the early Universe, such a SSD could also operate in other contexts, for example, in the subsonic environments of the lower solar corona as well as in the hot ionized interstellar medium of the galactic halo. It is, therefore, important to understand the SSD in the very subsonic regime.

A previous study by [21] has examined the properties of the dynamo as a function of the Mach number and the nature of turbulent driving. They have investigated the case when the SSD is driven solely by longitudinal modes for Mach numbers in the range $\mathcal{M} \sim 0.1$–20, thus not reaching

sufficiently far into the very subsonic regime relevant for the amplification of primordial magnetic fields. They also studied the case when the SSD is driven purely by solenoidal (or rotational) velocity modes for Mach numbers in the range $\mathcal{M} \sim 0.02$–20. We use the same setup as [21] for driving the turbulence in our study. We model the forcing term through the stochastic Ornstein-Uhlenbeck process, which determines the forcing field in the Fourier space. The definition of the forcing operator includes a projection in the Fourier space, which can project the forcing field onto solenoidal and compressive components [25].

When solenoidal modes are injected continuously in the plasma by the turbulent-forcing, vorticity is generated continuously in the plasma. The stretch-twist-fold (STF) mechanism of the SSD is more efficient when higher vorticity is present, as the magnetic field lines are twisted and folded more efficiently in this case. This, in turn, leads to faster amplification or growth rate of magnetic energy and a higher saturation efficiency of the SSD [21]. However, [21] only studied the properties of the purely solenoidally driven and purely compressively driven turbulence and did not consider cases with mixed forcing (solenoidal and longitudinal) of the turbulence. In this study, we determine the properties of the SSD with non-helical magnetic fields in the very subsonic regime for Mach numbers in the range $\mathcal{M} = 10^{-3}$–0.4 and for a wide range of turbulent driving conditions. We study the dynamo forced purely by longitudinal modes as well as for the case when the turbulent driving has both rotational and longitudinal modes (mixed forcing). Namely, we study the cases when the solenoidal fraction injected by the turbulent driving is 0% (purely compressive), 0.01%, 0.1%, 1% and 10%. We then apply our results to understand the amplification of primordial magnetic fields in the early Universe and discuss other applications of the highly subsonic SSD.

Chapter 2

Turbulent Amplification of Magnetic Fields

In this chapter, we discuss the basics of magnetohydrodynamics and turbulence. We build on these concepts further and describe the SSD, which can amplify magnetic fields exponentially. We then address the applications of the SSD and finally discuss it in the context of the amplification of primordial magnetic fields.

2.1   Magnetohydrodynamics

Magnetohydrodynamics is the study of conducting fluids or plasma, and their interaction with the magnetic field. In fluids, the frequent collisions at the molecular level helps to establish the macroscopic, observable properties of the fluid at much smaller length scales. For charged particles, even in the absence of collisions, magnetic fields can confine the particles and localize them, therefore establishing a fluid-like behavior. Plasma contains both positively charged ions and negatively charged electrons, but in magnetohydrodynamics, we consider plasma to be a single neutral fluid. We assume the charge separation between the positive ions and electrons to be negligible. This assumption is only valid if the length scales we are studying are larger than the Debye length, and the time scales of our study are larger than the inverse of the plasma frequency. So, we can not use Magnetohydrodynamics to study situations where there is considerable charge separation. We also assume that all transport coefficients in the plasma, for example, resistivity and viscosity are scalar and are isotropic. The material discussed in this sub-section can be found in [26] and [27].

2.1.1 MHD Equations

The Maxwell's equations in Gaussian cgs units are

$$\frac{1}{c}\frac{\partial \vec{B}}{\partial t} = -\nabla \times \vec{E} \tag{2.1}$$

$$\nabla \cdot \vec{B} = 0 \tag{2.2}$$

$$\nabla \cdot \vec{E} = 4\pi\rho \tag{2.3}$$

$$\frac{1}{c}\frac{\partial \vec{E}}{\partial t} = \nabla \times \vec{B} - \frac{4\pi}{c}\vec{J} \tag{2.4}$$

where $\vec{E}$ is the electric field, $\vec{B}$ is the magnetic field, $\vec{J}$ is the current density, ρ is the net charge density and c is the speed of light in vacuum. If we assume that there is no spontaneous change in the charge distribution, then $\partial \vec{E}/\partial t$ becomes zero and equation 2.4 reduces to

$$\nabla \times \vec{B} = \frac{4\pi}{c}\vec{J} \tag{2.5}$$

Using these fundamental equations, we can derive the induction equation which describes the evolution of the magnetic field in space and time.

Navier-Stokes equation for plasma

In the case of plasma, another force acts on the flow. This force is the Lorentz force that acts on charged particles. In astrophysical settings, the strength of the magnetic field is large enough to make a significant addition to the Navier-Stokes equation, and it has to be modified. The Lorentz force per unit volume can be written as

$$\vec{f_L} = q_i n_i \left(\vec{E} + \frac{1}{c} \vec{V_i} \times \vec{B} \right) - q_\varepsilon n_e \left(\vec{E} + \frac{1}{c} \vec{V_e} \times \vec{B} \right) \tag{2.6}$$

where n_i, q_i and $\vec{V_i}$ are the number density of the ions, charge on each of them and their drift velocity. n_e, q_e and $\vec{V_e}$ are the number density of the electrons, charge on the electron and the drift velocity of the electrons. The charge density, $\rho = q_i n_i - q_e n_e$ and the current density, $\vec{J} = q_i n_i \vec{V_i} - q_e n_e \vec{V_e}$. Using these relations, we get

$$\vec{f_L} = \rho \vec{E} + \frac{1}{c} \vec{J} \times \vec{B}$$

From the Maxwell's equations 2.3 and 2.5 we know that $\rho = \nabla \cdot \vec{E}/4\pi$ and $\vec{J} = c(\nabla \times \vec{B})/4\pi$. The ratio of the electric force and magnetic force is

$$\frac{\rho \vec{E}}{\frac{\vec{J} \times \vec{B}}{c}} = \frac{(\nabla \cdot \vec{E})\vec{E}}{(\nabla \times \vec{B})\vec{B}} \approx \frac{E^2}{B^2}$$

In the limit of infinite conductivity, $\vec{J}/\sigma$ becomes zero and from the Ohm's law, equation 2.13 , we get

$$\vec{E} = -\frac{\vec{V} \times \vec{B}}{c}$$

This implies

$$\frac{E^2}{B^2} \approx \frac{V^2}{c^2}$$

For non-relativistic fluids $V^2/c^2 \ll 1$ and so the magnetic force dominates the electric force. Ignoring the electric force and adding the magnetic body force, the Navier-Stokes equation becomes

$$\rho \left(\frac{\partial \vec{V}}{\partial t} + (\vec{V} \cdot \nabla)\vec{V} \right) = -\nabla P + \mu \nabla^2 \vec{V} + \frac{1}{c} \vec{J} \times \vec{B} + \vec{F_b} \tag{2.7}$$

$\vec{J}$ can be written in terms of the magnetic field from equation 2.5

$$\vec{J} = \frac{c}{4\pi} \nabla \times \vec{B} \tag{2.8}$$

Substituting this in equation 2.7 we have

$$\rho \left(\frac{\partial \vec{V}}{\partial t} + (\vec{V} \cdot \nabla)\vec{V} \right) = -\nabla P + \mu \nabla^2 \vec{V} + \frac{1}{4\pi}(\nabla \times \vec{B}) \times \vec{B} + \vec{F}_b \qquad (2.9)$$

and we know that

$$(\nabla \times \vec{B}) \times \vec{B} = (\vec{B} \cdot \nabla)\vec{B} - \nabla \left(\frac{\vec{B}^2}{2} \right) \qquad (2.10)$$

Substituting this into the equation 2.7 we get

$$\rho \left(\frac{\partial \vec{V}}{\partial t} + (\vec{V} \cdot \nabla)\vec{V} \right) = -\nabla P + \frac{1}{4\pi}(\vec{B} \cdot \nabla)\vec{B} - \frac{1}{4\pi}\nabla \left(\frac{\vec{B}^2}{2} \right) + \mu \nabla^2 \vec{V} + \vec{F}_b \qquad (2.11)$$

which can be re-written as

$$\rho \left(\frac{\partial \vec{V}}{\partial t} + (\vec{V} \cdot \nabla)\vec{V} \right) = -\nabla \left(P + \frac{\vec{B}^2}{8\pi} \right) + \frac{1}{4\pi}(\vec{B} \cdot \nabla)\vec{B} + \mu \nabla^2 \vec{V} + \vec{F}_b \qquad (2.12)$$

It is clear from equation 2.12 that the two terms introduced due to the magnetic field are very different. Magnetic field produces a pressure $\vec{B}^2/8\pi$ and the force due to the term $(\vec{B} \cdot \nabla)\vec{B}$ is similar to tension present in stretched strings.

Induction equation

The Ohm's law states that the current density, $\vec{J}$ in a region is directly proportional to the force acting per unit charge in that region

$$\vec{J} = \sigma \vec{f}$$

Where $\vec{f}$ is the force acting per unit charge, and σ is the conductivity. If the Lorentz force is driving the current, then the Ohm's law can be re-written as

$$\vec{J} = \sigma \left(\vec{E} + \frac{\vec{V} \times \vec{B}}{c} \right) \qquad (2.13)$$

14

Where $\vec{V}$ is the bulk velocity of the plasma. The electric field is a dependent variable and can be written in terms of $\vec{J}$ and $\vec{V}$. Substituting for $\vec{E}$ in the Faraday's law 2.1 and assuming that σ is spatially invariant we

$$\frac{\partial \vec{B}}{\partial t} = \nabla \times (\vec{V} \times \vec{B}) - \frac{c}{\sigma}(\nabla \times \vec{J}) \tag{2.14}$$

Taking the curl of equation 2.5 and substituting in the above equation, we get the Induction equation.

$$\frac{\partial \vec{B}}{\partial t} = \nabla \times (\vec{V} \times \vec{B}) + \eta \nabla^2 \vec{B} \tag{2.15}$$

where $\eta = c^2/4\pi\sigma$ is called the magnetic diffusivity.

The first term of the induction equation called the induction term is of the order VB/L, where L is the length scale of the system we are studying. The second term of the induction equation called the diffusion term is of the order $\eta B/L^2$. The ratio of these two terms is called the Magnetic Reynolds Number and is denoted by Rm.

$$Rm = \frac{LV}{\eta} \tag{2.16}$$

The magnetic Reynolds number, Rm, is very similar to Reynolds number of the flow, R_e. In laboratories the diffusion term dominates the induction term and Rm << 1. In such cases, the induction equation can be simplified to

$$\frac{\partial \vec{B}}{\partial t} = \eta \nabla^2 \vec{B} \tag{2.17}$$

The equation 2.17 describes this decay or diffusion of the magnetic field. So far, we have seven equations, three components of the induction equation, three components of the Navier-Stokes equation and the continuity equation. Including the energy equation, we have eight equations, and we have eight variables, the three components of the magnetic field, the three components of velocity, the pressure, and density. Hence, MHD is a complete dynamical theory with eight

variables and eight equations.

Flux Freezing

In astrophysical settings, unlike laboratories, the induction term dominates the diffusion term because the conductivity of plasma is infinite, or the diffusivity is zero and hence Rm >> 1. This condition is called the ideal MHD limit. This reduces the induction equation to

$$\frac{\partial \vec{B}}{\partial t} = \nabla \times (\vec{V} \times \vec{B}) \tag{2.18}$$

From Kelvin's Vorticity theorem, we have that for equations of such form

$$\frac{D}{Dt} \int \vec{B} \cdot \vec{ds} = 0 \tag{2.19}$$

This implies that $\int \vec{B} \cdot \vec{ds}$ is a constant or the flux of the magnetic field does not change in the ideal MHD limit. This means that the magnetic field is frozen into plasma. In the limit of infinite conductivity, if the orientation of the plasma is changed, then the orientation of the magnetic field also changes and vice-versa. This result is called the Alfvén's theorem.

One example of flux freezing is the large magnetic fields of compact astrophysical objects. When a star shrinks into a neutron star, in the limit of ideal MHD, the magnetic field of the parent star gets trapped in a much smaller volume. Since the flux of the magnetic field has to be conserved, the magnetic field strength of the neutron star has to be much larger than that of the parent star.

2.2   Small-Scale Dynamo

In this section, we describe the STF mechanism, followed by a discussion on the applications of the SSD.

2.2.1 Stretch-twist-fold Dynamo mechanism

The stretch-twist-fold (STF) mechanism of the SSD describes the exponential amplification of the magnetic energy by the SSD. This mechanism is illustrated in figure 2.1.
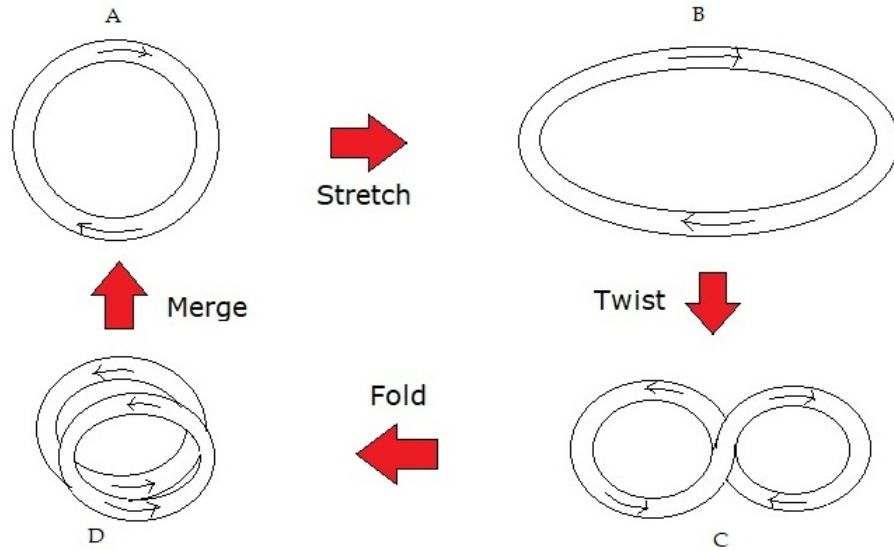
Figure 2.1: Illustration of the stretch-twist-fold model of the SSD

In the limit of ideal magnetohydrodynamics, the resistivity of the plasma can be taken to be vanishingly small. In this limit, we can assume that the magnetic flux is frozen into the plasma. We see this in the configuration A of figure 2.1. The first step in the amplification process is the stretching of this flux loop such that the circumference of the loop doubles. As the volume of the loop stays constant, the cross-section area of the loop is halved. Then from flux freezing, we have that the strength of the magnetic field doubles as the flux looped is stretched.

In the next step, the flux loop is twisted from configuration B to configuration C, and then the smaller loops are folded upon each other in configuration C to configuration D such that the magnetic field lines in both the smaller loops are parallel to each other. The presence of rotational motions in the plasma enhances these two steps making the dynamo more efficient. In the final step, the two smaller field loops merge (configuration D to configuration A) through the presence of some dissipative effects. This step is very crucial so as to make the process irreversible. In the final configuration, the cross-section area is equal to the first configuration; however, the magnetic field through the Eulerian cross-section doubles. The magnetic field strength is amplified by a factor of $\sim 2^n$ in n cycles of this process. This way, the SSD converts turbulent kinetic energy into magnetic

17

energy.

Growth rate of the SSD is dependent on the Pm and the nature of turbulence. For Pm >> 1 and Pm << 1, the growth rates of the SSD can be derived analytically using the Wentzel–Kramers–Brillouin (WKB) approximation for the Kazantsev equation [23, 28]. The saturation efficiencies and the saturation scale of the magnetic energy generated by the SSD also depend upon the Pm and this has been studied extensively for the limits Pm >> 1 and Pm << 1 by [24]. In the case of the early Universe, the Pm is high, and we use the results derived in [23] in the limit Pm → ∞ for the growth rate.

$$\Gamma = \frac{163 - 304\nu}{60} Re(L)^{(1-\nu)/(1+\nu)} \frac{V}{L} \tag{2.20}$$

In the above equation, ν captures the nature of turbulence. $\nu = 1/3$ corresponds to the incompressible Kolmogorov turbulence, and $\nu = 1/2$ corresponds to the compressible Burgers turbulence, and the Reynolds number is calculated at the length scale L.

2.2.2   Applications of the Small-Scale Dynamo

The SSD has a wide range of applications as it can operate in a variety of astrophysical situations. Studies by [29, 30, 31] have examined the effect of the SSD during the formation of the first stars. The SSD can amplify magnetic fields exponentially in the turbulent plasma when the magnetic Reynolds number (Rm) is above a critical value [23, 19]. Previous numerical studies have examined the SSD for a variety of parameters and in various astrophysical settings. The dynamo action depends on the kinetic Reynolds number (Re) and the Prandtl number (Pm) [22, 23, 28]. The properties of the SSD also depend on the Mach number of the flow. Previous studies have studied the properties of the SSD in the supersonic and transonic regime [21, 22]; however, it remains unexplored in the extremely subsonic regime. This regime is important for studies on magnetohydrodynamic turbulence and is relevant for many processes in astrophysics and cosmology, including the amplification of primordial magnetic fields. The energy injection by the turbulence, namely whether the forcing of the turbulence is solenoidal or compressive, effects the vorticity excited in the plasma. The amount of vorticity present in the velocity field is critical to the STF mechanism of the SSD [21] and therefore influences the amplification rate and the saturation efficiency of the dynamo.

2.3 Primordial magnetic fields

Turbulence can be generated in the early Universe during various phases through the first-order phase transitions and the primordial density perturbations [17]. In the early epochs, neutrinos are responsible for the transfer of heat and momentum and therefore determine the viscosity of the plasma. After the decoupling of the neutrinos at T=2.6 MeV, photons are responsible for the transfer of heat and momentum. We can divide the turbulent regimes in the early Universe into mainly two, before and after the decoupling of neutrinos. In case the turbulence is driven by primordial density fluctuations, density perturbations of the order of 10^{-5} can generate velocity fluctuations through its gravitational potential in the primordial plasma. This gives rise to velocity fluctuations of $\sim 5 \times 10^{-5}$ (in units with c=1) and a very low Mach number of $\sim 9 \times 10^{-5}$. In case first-order phase transitions occur in the early Universe, they can drive velocities of $10^{-4} - 10^{-1}$ leading to higher Mach numbers in the primordial plasma. We can define the turbulent driving scale, *L*, from the Hubble time of the Universe, making *L* the largest length scale possible for the turbulent driving.

The Re and Rm of the early Universe are determined from the quantities discussed above by [17]. As the Universe expands and cools, these quantities are a function of temperature and, therefore, a function of the age of the Universe. Considering the Reynolds number determined from the turbulence injected by the primordial density perturbations as a lower limit and that determined by turbulence injected through first-order phase transitions to be an upper limit, [17] derive the evolution of these quantities for temperatures in the range 100 MeV to 100 GeV.

When the stirring scales of the turbulence are larger than the damping scales of the neutrinos, and later on the damping scales of the photons, the plasma is turbulent with Re >> 1. For temperatures in the range 100 MeV to 100 GeV, [17] show that Re and Rm are sufficiently large and the Pm $\sim 10^2 - 10^{12}$. Below temperatures of 0.2 GeV, the neutrino damping length scales are bigger than the largest stirring scales causing the plasma to be viscous. Therefore, turbulence can be generated and can inject energy into the dynamo mechanism for temperatures between 0.2 GeV to 100 GeV [17]. We calculate the growth rate from Equation 2.20 at the largest possible stirring scale, *L*. In our case, Γ is a function of time as the Reynolds number changes when the Universe expands.

The magnetic energy amplification by the SSD is exponential and is determined by the equation $E_{\mathrm{m}}/E_{\mathrm{m0}} = e^{\Gamma(\mathrm{t})t}$. By performing the integral $\int \Gamma(\mathrm{t})dt$ over the appropriate time in the Universe, we can determine the number of e-foldings. [17] determine the evolution of this integral in the primordial Universe and show that sufficient time in terms of turn-over time is possible in the early

Universe for the SSD action. [17] conclude that through the turbulence driven by primordial density perturbations, magnetic fields with strengths $10^{-15}((E_{\text{mag}}/E_{\text{kin}})_{\text{sat}})^{1/2}$ Gauss can be generated on scales of 0.1 pc. In the case when the turbulence driven by first-order phase transitions, significantly higher magnetic fields with strengths $10^{-12}((E_{\text{mag}}/E_{\text{kin}})_{\text{sat}})^{1/2}$ can be generated on scales of 100 pc.

Chapter 3

Methods

In this chapter, we discuss the code we use for simulating the SSD - the FLASH code, which solves the compressible magnetohydrodynamic equations. We first discuss the equations that are solved by the FLASH code, followed by a detailed discussion on how we implement the SSD problem using the FLASH code. We then describe the quantities relevant to our study and discuss how we measure them.

3.1   Simulation code

We model the SSD using the FLASH code and compute the solutions numerically. The FLASH code solves the following 3-dimensional magnetohydrodynamical equations [32]

$$\frac{\partial \rho}{\partial t} + \nabla \cdot (\rho \vec{v}) = 0 \tag{3.1}$$

$$\frac{\partial (\rho \vec{v})}{\partial t} + \nabla \cdot (\rho \vec{v} \otimes \vec{v} - \vec{B} \otimes \vec{B}) + \nabla p = \nabla \cdot (2\nu \rho S) + \rho \vec{f} \tag{3.2}$$

$$\frac{\partial \vec{B}}{\partial t} = \nabla \times (\vec{v} \times \vec{B}) + \eta \nabla^2 \vec{B}, \tag{3.3}$$

with $\nabla \cdot \vec{B} = 0$. Here ρ, $\vec{v}$ and $\vec{B}$ are the density, velocity and the magnetic field respectively, while ν and η are the kinematic viscosity and the magnetic resistivity. The set of equations are completed with the isothermal equation of state, $p = c_s^2 \rho$ where, c_s is the speed of sound. The total pressure p is the sum of the magnetic and thermal pressure of the system, $p = p_{thermal} + (1/2)|\vec{B}|^2$. While S captures the viscous interactions, $S_{ij} = (1/2)(\partial_i v_j + \partial_j v_i) - (1/3)\delta_{ij}\nabla \cdot \vec{v}$ and $\vec{f}$ is the turbulent forcing field that drives the dynamo, which feeds kinetic energy continuously to the dynamo. This forcing field is modelled using a stochastic Ornstein-Uhlenbeck process, which is discussed later on.

3.2   Small-scale dynamo Simulations

The SSD is driven by the turbulence in the plasma, which is instigated at large length scales, creating eddies at these length scales. These eddies then decay into smaller eddies, which then break down into even smaller eddies, hence creating a cascade of energy from larger length scales to smaller length scales [33]. This cascade of eddies continues to the dissipative scale or the viscous scale where they decay. The eddies generated at the smaller length scales amplify the magnetic field through the STF mechanism [19]. The stretch twist fold mechanism amplifies the magnetic field exponentially, $E_m/E_{m0} = \exp(\Gamma t)$, where E_m is the magnetic energy density, E_{m0} is the initial magnetic energy density, Γ is the growth rate and t is time, normalised to the eddy-turn over time (t_{ed}). The eddy turn over time is given by $t_{ed} = L/V$, where L is the length scale at which turbulence is driven, and V is the velocity corresponding to this length scale.

3.2.1   Ornstein-Uhlenbeck Process

The following stochastic differential equation models the Ornstein-Uhlenbeck process. It determines the evolution of $\vec{f}$ in Fourier space [25]

$$d\vec{f}(\vec{k}, t) = f_0(\vec{k})\mathcal{P}^\zeta(\vec{k})dW(t) - \vec{f}(\vec{k}, t)\frac{dt}{T},$$

(3.4)

where $\mathcal{P}^\zeta(\vec{k})$ is the projection operator which contains the curl-free compressive projection $\mathcal{P}^{\parallel}_{ij} =$

$k_i k_j/k^2$ and the divergence-free solenoidal projection $\mathcal{P}^\perp_{ij} = \delta_{ij} - k_i k_j/k^2$ of the driving.

$$\mathcal{P}^\zeta(\vec{k}) = \zeta \mathcal{P}^\perp_{ij}(\vec{k}) + (1 - \zeta)\mathcal{P}^\parallel_{ij}(\vec{k}). \tag{3.5}$$

From the above equation, we see $\zeta = 0$ leads to curl-free or purely compressive driving as $\nabla \times \vec{f} = 0$ in this case. $\zeta = 1$ leads to divergence-free or purely solenoidal forcing of the turbulence as in this case $\nabla \cdot \vec{f} = 0$. [21] have shown that the behavior of the SSD is very different in both these cases for sub-sonic turbulence. Solenoidal driving excites more vorticity in the plasma, and vorticity helps the STF mechanism of the dynamo to amplify the magnetic field more efficiently [21, 30].

We control the Mach number ($\mathcal{M} = V/c_s$) by adjusting the forcing field. As the dynamo requires a seed magnetic field, we set an initial magnetic field corresponding to an initial plasma beta $\beta = 2p_{\text{thermal}}/B^2 = 10^{10} - 10^{14}$. We solve the continuity equation (3.1), momentum equation with the forcing field (3.2), the induction equation (3.3) simultaneously with the isothermal equation of state to simulate the SSD.

3.2.2   Small-Scale Dynamo simulations

In this subsection, we define and discuss some important quantities and parameters relevant to our study of the SSD.

- Mach number ($\mathcal{M}$) is defined as $\mathcal{M} = V/c_s$, where V is the plasma velocity and c_s is the sound speed. We determine the Mach number in our simulations by calculating the average over a few initial turn-over times ($\sim 3t_{\text{ed}} - 20t_{\text{ed}}$) and determine the error on the Mach number by calculating the standard deviation over these initial turn-over times.

- Turn-over time (t_{ed}) is defined as the time-scale in which eddies at a particular length (L) scale pass on their energy to eddies at smaller length scales. $t_{\text{ed}} \sim L/V$, where V is the velocity at this length scale. This time scale is relevant to the time scales at which the dynamo amplification takes place. In this study, we define it to be the turn-over time of the eddies at the peak driving scale ($L/2$). This gives us $t_{\text{ed}} = L/2V$ or $t_{\text{ed}} = L/(2\mathcal{M}c_s)$.

- Growth (or amplification) rate (Γ) is the rate at which the turbulent SSD amplifies magnetic

energy. We determine this quantity by an exponential fit function in time to the magnetic energy in the amplification phase of the SSD before the saturation level is attained.

- $E_{\mathrm{mag}}/E_{\mathrm{kin}}$ is the ratio of the magnetic energy (E_{mag}) to the kinetic energy (E_{kin}). E_{kin} in the simulations is constant and does not change after the initial phase. E_{mag}, however, increases exponentially in time.

- $E_{\mathrm{m}}/E_{\mathrm{m0}}$ is the ratio of the magnetic energy to the initial average magnetic energy of the plasma. The initial magnetic energy is set to be small compared to the kinetic energy of the plasma so that we can observe the magnetic field amplification by the SSD.

- $(E_{\mathrm{mag}}/E_{\mathrm{kin}})_{\mathrm{sat}}$ is the saturation efficiency of the SSD. It is the value of the ratio $E_{\mathrm{mag}}/E_{\mathrm{kin}}$ after the SSD action has saturated. $(E_{\mathrm{mag}}/E_{\mathrm{kin}})_{\mathrm{sat}}$ quantifies the efficiency with which the turbulent kinetic energy is converted to E_{mag} by the SSD and is, therefore, a significant quantity. We calculate $(E_{\mathrm{mag}}/E_{\mathrm{kin}})_{\mathrm{sat}}$ by taking an average of $E_{\mathrm{mag}}/E_{\mathrm{kin}}$ in the regime where the SSD has saturated and determined the error on the saturation efficiency by calculating the standard deviation over these time intervals.

- $E_{\mathrm{sol}}/E_{\mathrm{tot}}$ is the solenoidal fraction in the kinetic energy. It is calculated by performing a Helmholtz projection of the velocity field to determine the energy in the rotational (or curl) modes and the compressive (or divergence) modes and then taking the ratio of the energy in the rotational modes to the total kinetic energy. $E_{\mathrm{sol}}/E_{\mathrm{tot}}$ determines the vorticity present qualitatively in the plasma and is correlated to the growth rate of the SSD.

Chapter 4

Results and Discussion

4.1 Preliminary Results

We performed our initial simulations by solving the complete set of non-ideal magnetohydrodynamic equations, including viscosity and resistivity. We execute this by implementing the viscosity and resistivity modules in the FLASH code. The kinetic Reynolds number, Re, is determined by LV/v where v is the viscosity, L is the relevant length scale, and V is the velocity at this length scale. The magnetic Reynolds number, Rm, is determined by LV/η where η is the resistivity, L is the relevant length scale, and V is the velocity at this length scale. Re and Rm can be varied by changing the coefficients of v and η.

As discussed in the earlier sections, the properties of the SSD depend on the Reynolds numbers [22, 23, 28]. We study the purely compressively driven SSD with a Mach number of ~ 0.1. We fix the Re ~ 1500 and vary Pm by changing the magnetic Reynolds number.

From figure 4.1, we see that for Pm between 1 to 10, the saturation efficiency is highly dependent on the magnetic Reynolds number in our simulations. At higher Prandtl numbers, the numerical viscosity and resistivity due to the grid discretization start to influence the Reynolds numbers being implemented in our simulations. In the early Universe, Pm ~ $10^2 - 10^{12}$) which is higher than what can be achieved in the simulations [17]. The Reynolds numbers in the early Universe are also very high, and such numbers are not realized in our simulations.
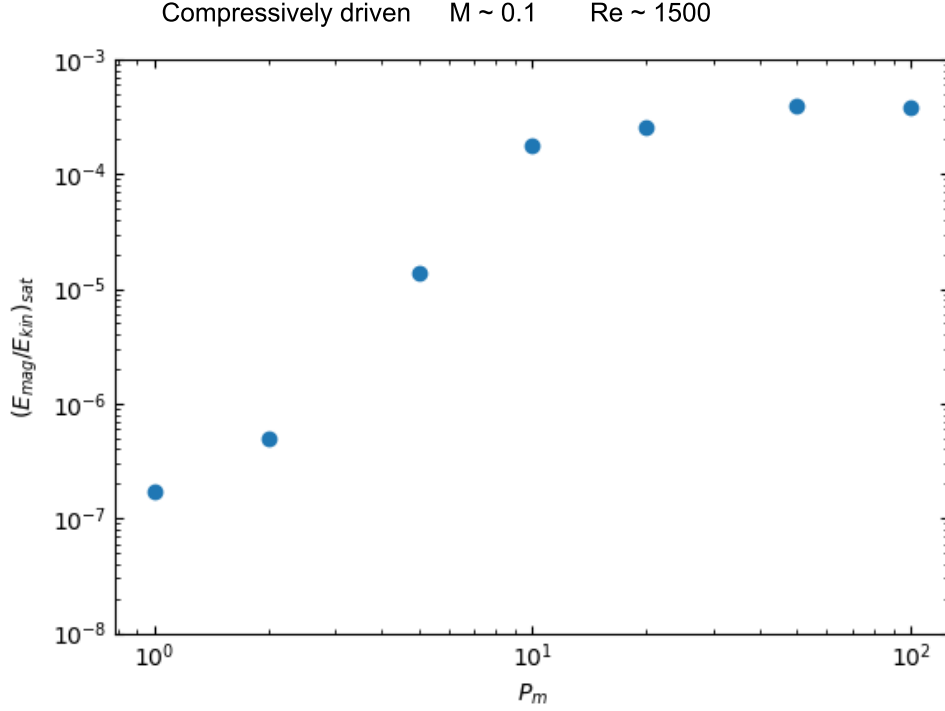
Figure 4.1: Non-ideal MHD simulations with fixed Reynolds number ($\sim$ 1500) and Mach number of 0.1 for the purely compressively driven dynamo. The figure shows the saturation efficiency, $(E_{\mathrm{mag}}/E_{\mathrm{kin}})_{\mathrm{sat}}$, of the SSD as a function of Pm.

For all future simulations, we resort to performing ideal MHD simulations where the resistivity and viscosity modules are not implemented. In this case, Re and Pm are determined by the numerical viscosity and resistivity in the simulations. The Pm $\sim$ 1 in our simulations.

4.2 Turbulent and Mean Initial Fields

As discussed earlier, the presence of an initial seed feed is necessary for the dynamo action to begin. To understand how the nature of the initial seed field influences the properties of the SSD, we set up a turbulent initial seed field, which has a no mean direction in addition to the previously used mean-initial field, for some of our low-Mach number simulations.

Figure 4.2 shows the evolution of the magnetic energy for simulations with a mean initial field and turbulent initial field. The green and blue curves are simulations with $\mathcal{M} \sim 0.1$ for a mean initial field and a turbulent initial field, respectively. The red and orange curves are simulations with
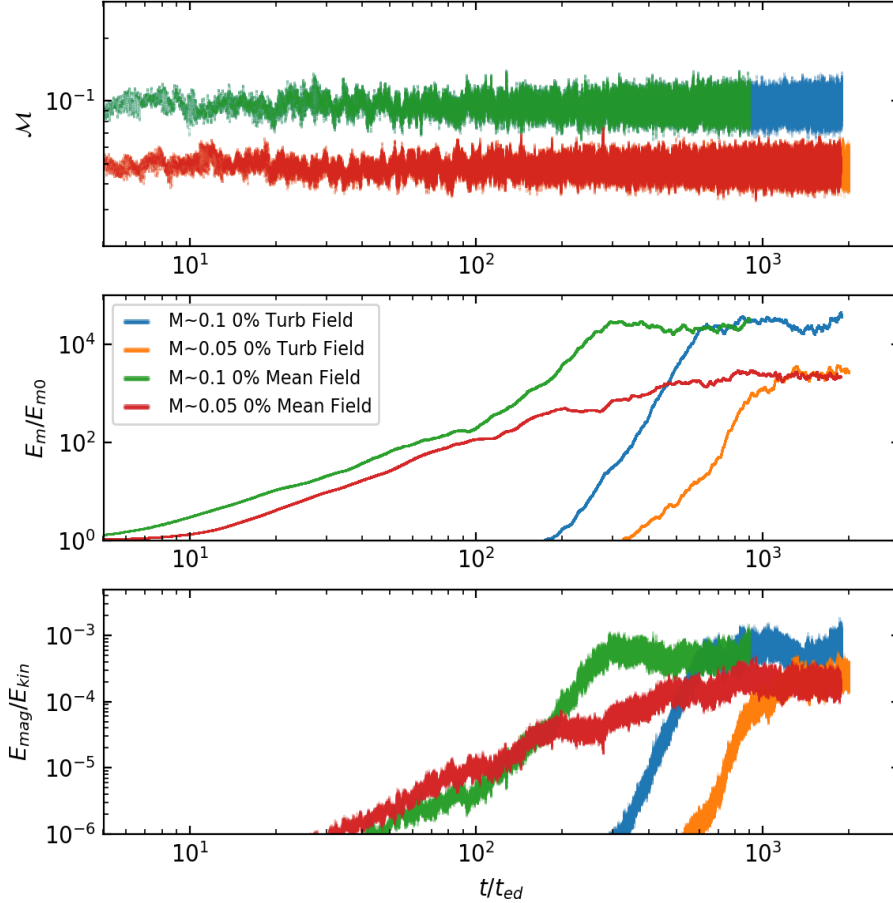
Figure 4.2: Mach number (top panel); $E_{\mathrm{m}}/E_{\mathrm{m0}}$ (middle panel) and $E_{\mathrm{mag}}/E_{\mathrm{kin}}$ (bottom panel) evolution for the above simulations. Time is normalized to the t_{ed} at the largest scales. We study models with $\mathcal{M} \sim 0.05$ and 0.1 with purely compressive driving for the cases when the initial magnetic seed field is a mean-field and a turbulent field.

$\mathcal{M} \sim 0.05$ for a mean initial field and a turbulent initial field, respectively. We see that for both the Mach numbers we have studied, the saturation point of the SSD is independent of the nature of the initial seed field. The principal difference between these two cases is the initial evolution of E_{mag}.

Until now, we have only studied cases where the SSD is driven solely by longitudinal velocity modes. Now, we consider the case when the turbulent forcing injects solenoidal velocity modes continuously as well (ζ lies between 0 and 1). In this section, we consider the case when $\zeta = 0.1$, $\zeta = 0.01$ and $\zeta = 0.001$. To understand how the nature of the initial field influences the dynamo amplification, we perform all the simulations shown below with both types of initial seed fields.

From Figure 4.3 and 4.4, it is clear that increasing the solenoidal fraction in the turbulent forcing
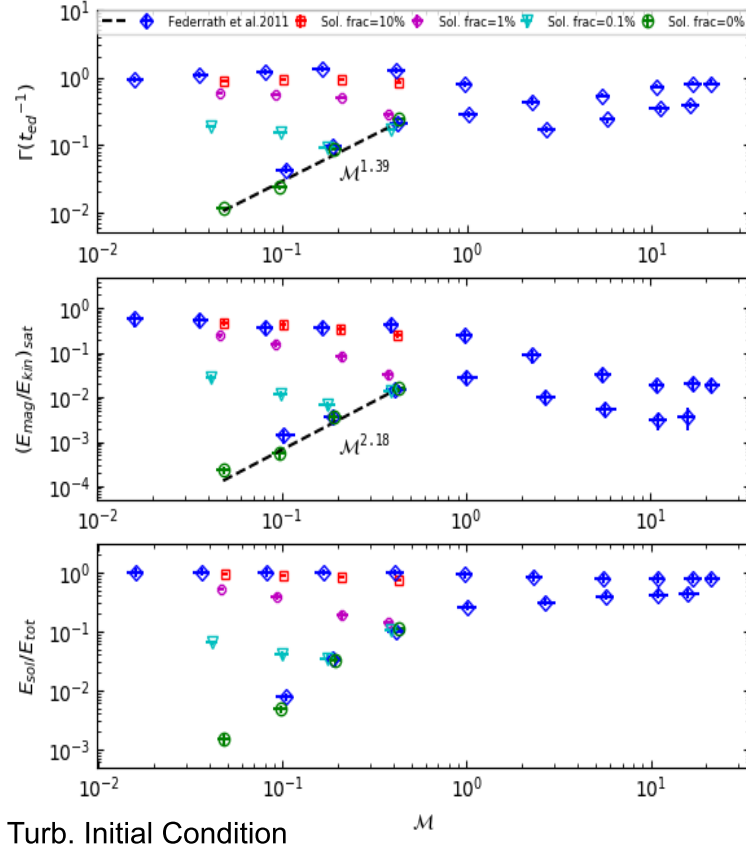
Figure 4.3: Growth rate (top panel); $(E_{\mathrm{mag}}/E_{\mathrm{kin}})_{\mathrm{sat}}$ (middle panel) and $E_{\mathrm{sol}}/E_{\mathrm{tot}}$ (bottom panel) as a function of $\mathcal{M}$ for the case when the initial magnetic seed field is turbulent.
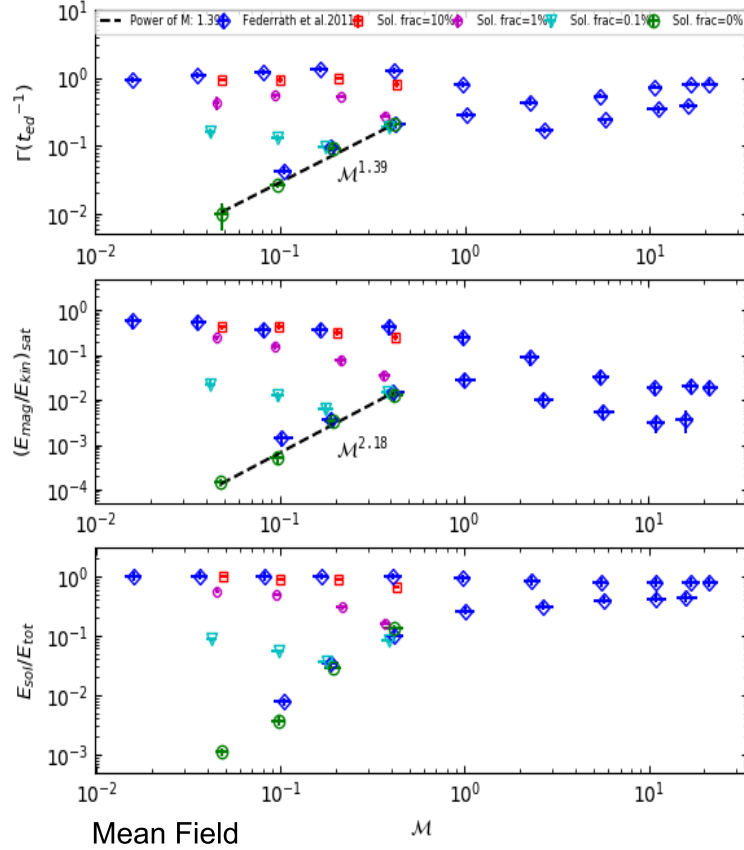
Figure 4.4: Growth rate (top panel); $(E_{\mathrm{mag}}/E_{\mathrm{kin}})_{\mathrm{sat}}$ (middle panel) and $E_{\mathrm{sol}}/E_{\mathrm{tot}}$ (bottom panel) as a function of $\mathcal{M}$ for the case with a mean initial seed magnetic field.

increases the $(E_{\mathrm{mag}}/E_{\mathrm{kin}})_{\mathrm{sat}}$ and Γ of the dynamo. This is because the amount of vorticity present in the plasma is critical to the SSD action and, therefore, $E_{\mathrm{sol}/E_{\mathrm{tot}}}$ is consequential to the behavior of the dynamo. We also fit power laws to the Γ and $(E_{\mathrm{mag}}/E_{\mathrm{kin}})_{\mathrm{sat}}$ of the dynamo for the purely compressively driven case. From our findings, illustrated in Figure 4.3 and 4.4, we find that the properties of the dynamo are independent of the nature of the seed field. We can also see that the properties of the dynamo depend on $\mathcal{M}$ and the nature of turbulent driving.

However, in the case with the initial seed field having a mean direction, we find a steeper growth rate in the beginning, because of the tangling up of magnetic field lines during the initial phase. This can affect the estimation of the growth rate. With an initial turbulent magnetic field, the magnetic field decays initially for a short while until the dynamo action sets in, increasing the magnetic energy exponentially. To obtain a better estimation of the growth rate of the magnetic energy due to the SSD, we use a turbulent initial seed field for all future simulations. The saturation efficiency of

the SSD is, however, independent of this, as we have seen above.

4.3   Simulations with Initial Vorticity
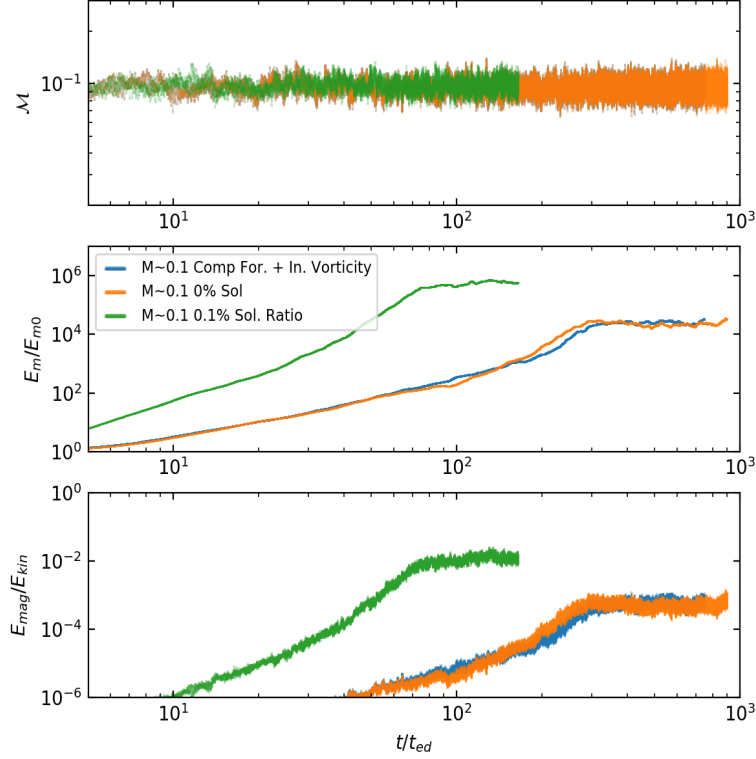
Figure 4.5: Mach number (top panel); $E_{\mathrm{m}}/E_{\mathrm{m0}}$ (middle panel) and $E_{\mathrm{mag}}/E_{\mathrm{kin}}$ (bottom panel) evolution for the above simulations. Time is normalized to the t_{ed} at the largest scales. We study models with $\mathcal{M} \sim 0.1$ for purely compressive driving (orange curve), with purely compressive forcing and initial vorticity present in the plasma (blue curve) and a solenoidal component of 0.1% ($\zeta = 0.001$) present in the forcing (green curve).

From our results so far, it is clear that the amount of vorticity present in the plasma is significant to the dynamo action. We, therefore, investigate this in greater detail. To understand if the presence of rotational motions at the beginning of the simulations affects the dynamo, we set up simulations with initial turbulent motions (or vorticity) in the plasma. This is independent of the way we implement the forcing of the turbulence, which occurs continuously throughout the simulations.

In Figure 4.5, the orange curve depicts the time evolution purely compressively driven simulation. The green curve corresponds to the dynamo driven with constant a solenoidal fraction in the driving

field ($\zeta = 0.001$), and the blue curve depicts the simulations with purely compressive forcing and initial rotational motions present in the plasma. We find that the presence of initial vorticity does not affect the growth rate and the $(E_{\mathrm{mag}}/E_{\mathrm{kin}})_{\mathrm{sat}}$ of the dynamo. The turbulent rotational motions injected at the beginning of the simulations decay quickly, and the turbulent forcing then takes over. It is also clear that the injection of solenoidal velocity modes continuously by the forcing has a significant effect on the dynamo properties. For example, the saturation efficiency of the dynamo increases by more than an order of magnitude when a solenoidal fraction of 0.1% ($\zeta = 0.001$) is introduced in the forcing.

4.4   Vorticty

We study the properties of the turbulent SSD in the subsonic regime, $\mathcal{M} \sim 10^{-3}$-0.4. [21] have shown that the properties of the turbulent-dynamo depend critically on the solenoidal (rotational) or compressive (longitudinal) nature of turbulent driving. A dynamo driven by solenoidal forcing shows a higher amplification rate and saturation efficiency because, in this case, the driving field injects vorticity directly into the plasma, which is then able to drive the STF mechanism of the SSD efficiently. However, with compressive forcing, solenoidal modes are not injected directly by the turbulent driving, and the plasma might have zero initial vorticity.

We analyze the vorticity and the divergence of the velocity field obtained in these simulations. Figure 4.6 shows the root mean square (rms) value of the magnitude of vorticity averaged over all grid cells for our simulations with $\mathcal{M} \sim 10^{-3} - 0.4$. Figure 4.7 shows the rms value of the magnitude of divergence of the velocity field averaged over all grid cells for our simulations with $\mathcal{M} \sim 10^{-3} - 0.4$. We see that the vorticity and the divergence of the velocity field decrease with the Mach number. This result is expected because we achieve lower Mach numbers in our simulations by reducing the energy injected into the velocity field by the turbulent forcing.

However, it is more interesting to investigate the energies in the rotational kinetic modes. The energy in the kinetic energy modes are present in the rotational or vorticity ($\nabla \times \vec{v}$) modes and the compressive or divergence ($\nabla \cdot \vec{v}$) modes. The energy in the solenoidal or rotational modes can be represented by $\sim (\nabla \times \vec{v})^2/((\nabla \times \vec{v})^2 + (\nabla \cdot \vec{v})^2)$ and the energy in the compressive or longitudinal modes can be represented by $\sim (\nabla \cdot \vec{v})^2/((\nabla \times \vec{v})^2 + (\nabla \cdot \vec{v})^2)$. Figure 4.8 shows the rms value of the kinetic energy in rotational modes, $((\nabla \times \vec{v})^2/((\nabla \times \vec{v})^2 + (\nabla \cdot \vec{v})^2))$, averaged over all grid cells for our simulations with $\mathcal{M} \sim 10^{-3} - 0.4$. This ratio decreases until $\mathcal{M} \sim 0.05$ and then increases again
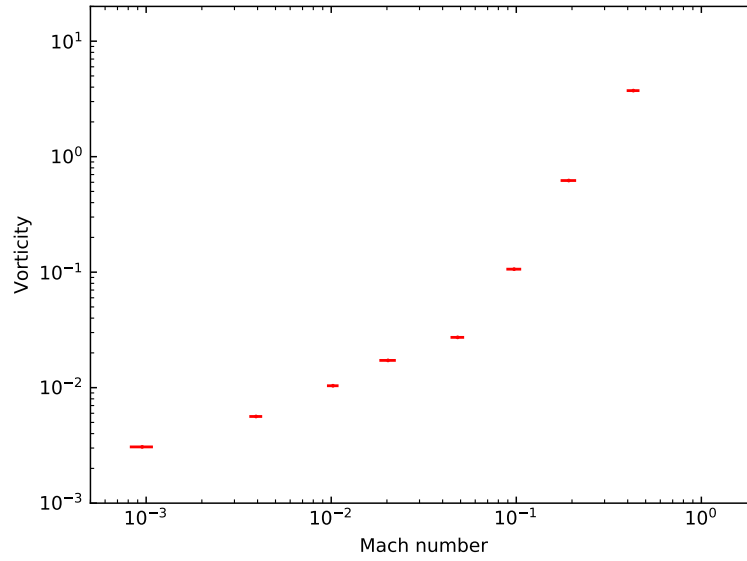
Figure 4.6: Vorticity for Mach numbers between $10^{-3} - 0.4$ for the purely compressively driven SSD
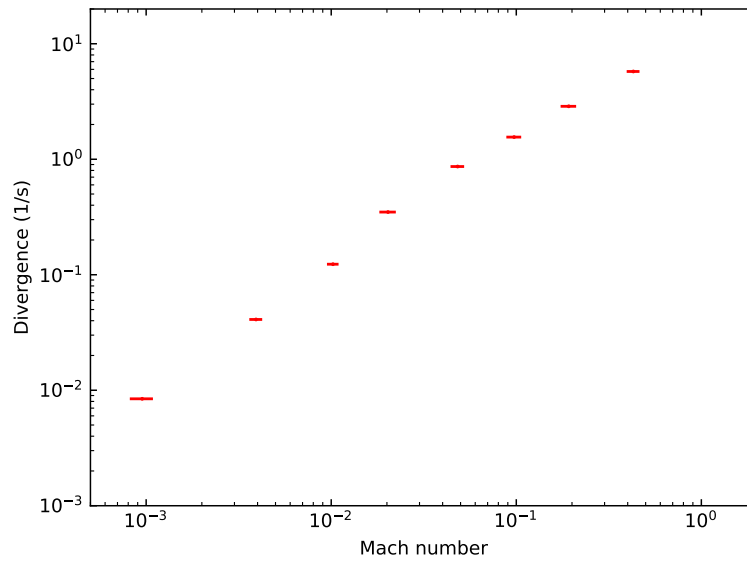
Figure 4.7: Divergence of the velocity field for Mach numbers between $10^{-3} - 0.4$ for the purely compressively driven SSD

as the Mach number decreases.
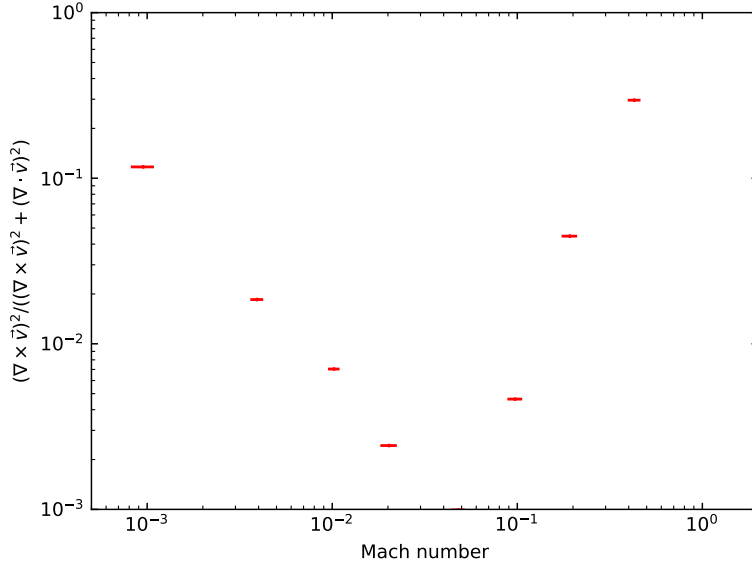
Figure 4.8: Ratio of the energy in solenoidal velocity modes to the total kinetic energy for Mach numbers between $10^{-3} - 0.4$ for the purely compressively driven SSD

Before we present and discuss our numerical results, we briefly address the basic equation for the evolution of vorticity. Vorticity, defined as $\vec{\omega} = \nabla \times \vec{v}$, follows the evolution equation [34]

$$\frac{\partial \vec{\omega}}{\partial t} = \nabla \times (\vec{v} \times \vec{\omega}) + \nu \nabla^2 \vec{\omega} + \frac{1}{\rho^2} \nabla \rho \times \nabla p + 2\nu \nabla \times S \nabla \ln \rho. \tag{4.1}$$

The vorticity equation has the same structure as the induction equation (3.3) and can therefore give rise to an exponential growth of vorticity similar to the amplification of magnetic fields by the SSD, if the last three terms on the R.H.S of equation (4.1) are subdominant compared to the first term [23]. Considering we start with zero initial vorticity, the baroclinic term $(\nabla \rho \times \nabla p)/\rho^2$ can not generate any vorticity, as the system is isothermal and we have $p = c_s^2 \rho$. However, if density gradients are present, then through viscous interactions, the last term on the R.H.S of equation (4.1) can generate vorticity, which can then be amplified through the first term on the R.H.S of equation (4.1).

4.5   Time Evolution

Figure 4.9 depicts the evolution of the Mach number, E_m/E_{m0}, and E_{mag}/E_{kin} as a function of time (normalized to the turn-over time (t_{ed})) for a representative sample of our low Mach number simulations. The middle panel shows the exponential amplification of E_{mag} by the SSD, and the bottom panel shows how the E_{mag} grows and saturates relative to the kinetic energy.

4.6   Dynamo growth rates and saturation levels

The amplification rate (Γ), the saturation efficiency (($E_{mag}/E_{kin})_{sat}$), and the solenoidal fraction in the kinetic energy (E_{sol}/E_{tot}) for all the turbulent driving models we have studied are shown in figure 4.10. The solenoidal fraction of the E_{kin} is correlated to the amplification rate, Γ. The higher the solenoidal modes in the velocity field, the higher the vorticity of the plasma, which leads to a more efficient amplification of the magnetic energy and, therefore, a higher amplification rate. We find that for purely compressive driving, the amplification rate and the saturation efficiency decline with the Mach number until $\mathcal{M} \sim 0.05$. Below this Mach number, it is easier for the energy injected by the turbulence to drive rotational modes, thus generating relatively more vorticity in the plasma and increasing the solenoidal fraction of E_{kin}. The dynamo is very sensitive to the solenoidal fraction of the E_{kin}, and as E_{sol}/E_{tot} increases, the amplification rate and $(E_{mag}/E_{kin})_{sat}$ of the dynamo increase. In the very subsonic regime, both E_{sol}/E_{tot} and $(E_{mag}/E_{kin})_{sat}$ increase as the Mach number decreases.

With a solenoidal fraction of 0.1 in the driving, we find that the saturation efficiency approaches the results from [21] for purely solenoidal driving. This is also observed for the dynamo with solenoidal fractions of 0.01 and 0.001 in the forcing. With a solenoidal fraction of 0.0001, we find that at $\mathcal{M} \sim 10^{-3}$, the saturation efficiency increases by order of magnitude compared to the dynamo driven by purely compressive driving ($\zeta = 0$). We also perform the low Mach number simulations with solenoidal fractions of 0.001 and 0.01 on 256^3, 512^3, and 576^3 grid cells and show that the value of the saturation efficiency converges with resolution.

We use the following function to model the saturation efficiency and the solenoidal fraction in the $(E_{mag}/E_{kin})_{sat}$ as a function of the $\mathcal{M}$
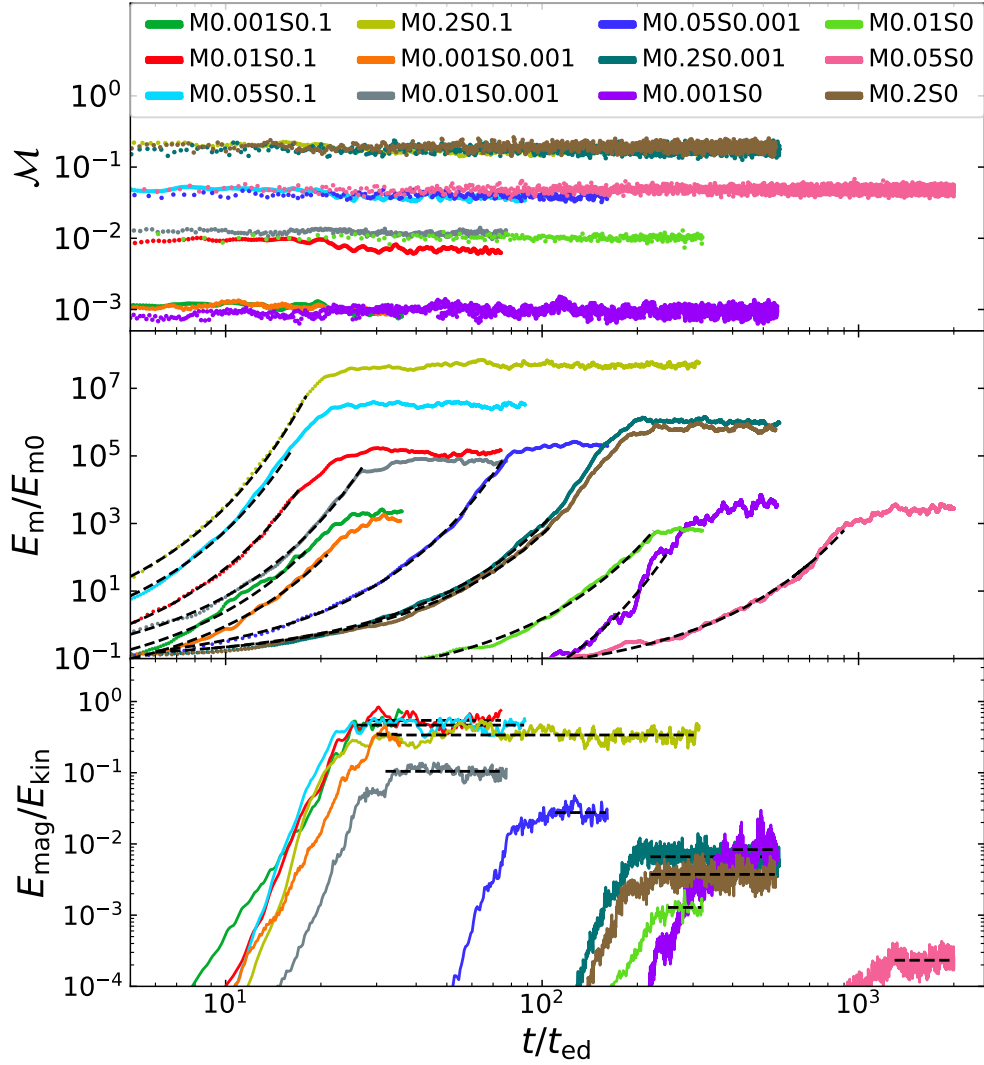
Figure 4.9: Mach number (top panel), magnetic energy, E_m/E_{m0} (middle panel), and saturation level, E_{mag}/E_{kin} (bottom panel) as a function of t_{ed} for a representative sample of our low Mach number simulation models on 128^3 grid cells with solenoidal fraction of 0.1, 0.001 and 0 (purely compressive) in the forcing. In the model name "M" stands for the Mach number, and "S" stands for the solenoidal fraction (ζ) in the driving field. The dotted lines in the middle panel show the fits for the amplification rate. The dotted black lines in the bottom panel show the fits for the saturation efficiency.
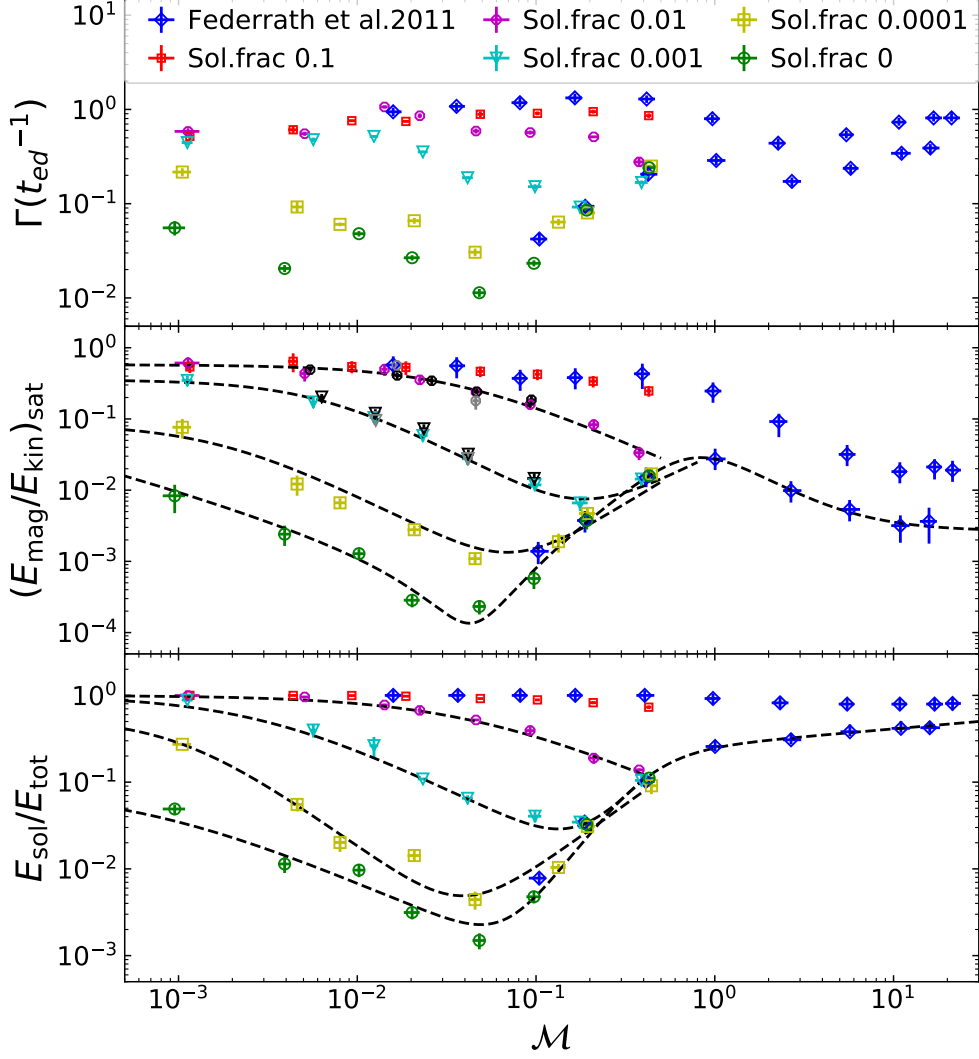
Figure 4.10: Amplification rate, Γ (top panel), Saturation efficiency, $(E_{mag}/E_{kin})_{sat}$ (middle panel) and E_{sol}/E_{tot} (bottom panel) as a function of Mach number for solenoidal fraction (ζ) of 0.1, 0.01, 0.001, 0.0001 and 0 in the turbulent driving. Dark blue (diamond) data points show purely compressive and purely solenoidal driving cases taken from Figure 3 in [21]. The dotted black lines show the fits to the data to guide the eye. The black data points in the middle panel correspond to the simulations done on 256^3 grid cells for $\zeta = 0.01$ and $\zeta = 0.001$. The grey data points at $\mathcal{M} \sim$ 0.01 and 0.05 in the middle panel correspond to simulations done on 512^3 grid cells (for $\zeta = 0.01$) and 576^3 grid cells (for $\zeta = 0.001$).

Table 4.1: Fit parameters for the saturation efficiency and the solenoidal ratio of the kinetic energy modelled in equation 4.2 for purely compressive driving (shown in Figure 4.10)

	$(E_{\mathrm{mag}}/E_{\mathrm{kin}})_{\mathrm{sat}}$	$E_{\mathrm{sol}}/E_{\mathrm{tot}}$
p_1	3.605×10^{-2}	2.735×10^{-1}
p_2	1.878×10^{0}	2.794×10^{0}
p_3	-3.734×10^{-2}	0
p_4	3.483×10^{0}	2.616×10^{0}
p_5	4.043×10^{-1}	1.086×10^{-1}
p_6	1.870×10^{-1}	2.066×10^{-2}
p_7	-7.770×10^{-1}	-1.011×10^{0}
p_8	-7.770×10^{-1}	-7.282×10^{-1}
p_9	3.793×10^{3}	3.272×10^{2}
p_{10}	2.695×10^{-3}	0

Table 4.2: Fit parameters for the saturation efficiency and the solenoidal ratio of the kinetic energy modelled in equation 4.2 for $\zeta = 0.0001$ (shown in Figure 4.10)

	$(E_{\mathrm{mag}}/E_{\mathrm{kin}})_{\mathrm{sat}}$	$E_{\mathrm{sol}}/E_{\mathrm{tot}}$
p_1	8.520×10^{-2}	5.525×10^{-1}
p_2	-1.286×10^{0}	-1.493×10^{0}
p_3	0	0
p_4	-1.286×10^{0}	-1.493×10^{0}
p_5	3.606×10^{3}	2.866×10^{4}
p_6	3.777×10^{-2}	3.068×10^{-1}
p_7	1.543×10^{0}	1.488×10^{0}
p_8	0	0
p_9	0	0
p_{10}	0	0

$$f(\mathcal{M}) = \frac{p_1(\mathcal{M}^{p_2} + p_3)}{\mathcal{M}^{p_4} + p_5} + \frac{p_6 \mathcal{M}^{p_7}}{\mathcal{M}^{p_8} + p_9} + p_{10} \tag{4.2}$$

The fit parameters are presented in table 4.1 (for $\zeta = 0$), table 4.2 (for $\zeta = 0.0001$), table 4.3 (for $\zeta = 0.001$) and table 4.4 (for $\zeta = 0.01$). The corresponding fits are shown in Figure 4.10. It is clear that in the very subsonic regime, $(E_{\mathrm{mag}}/E_{\mathrm{kin}})_{\mathrm{sat}}$ and $E_{\mathrm{sol}}/E_{\mathrm{tot}}$ increase as the Mach number decreases and ultimately saturate close to a value of 1.

The density fluctuations in the plasma decrease with the Mach number leading to the decline in the density gradients. This, in turn, enables the first term on the R.H.S of equation (4.1) to operate

Table 4.3: Fit parameters for the saturation efficiency and the solenoidal ratio of the kinetic energy modelled in equation 4.2 for $\zeta = 0.001$ (shown in Figure 4.10)

	$(E_{\mathrm{mag}}/E_{\mathrm{kin}})_{\mathrm{sat}}$	$E_{\mathrm{sol}}/E_{\mathrm{tot}}$
p_1	3.548×10^{-1}	5.525×10^{-1}
p_2	-1.361×10^{0}	-1.493×10^{0}
p_3	0	0
p_4	-1.361×10^{0}	-1.493×10^{0}
p_5	9.556×10^{2}	2.866×10^{4}
p_6	3.200×10^{-2}	3.068×10^{-1}
p_7	1.253×10^{0}	1.488×10^{0}
p_8	0	0
p_9	0	0
p_{10}	0	0

Table 4.4: Fit parameters for the saturation efficiency and the solenoidal ratio of the kinetic energy modelled in equation 4.2 for $\zeta = 0.01$ (shown in Figure 4.10)

	$(E_{\mathrm{mag}}/E_{\mathrm{kin}})_{\mathrm{sat}}$	$E_{\mathrm{sol}}/E_{\mathrm{tot}}$
p_1	8.207×10^{-3}	1
p_2	1.991×10^{-1}	-9.160×10^{-1}
p_3	0	0
p_4	1.173×10^{0}	-9.160×10^{-1}
p_5	4.708×10^{-2}	1.664×10^{1}
p_6	0	0
p_7	0	0
p_8	0	0
p_9	0	0
p_{10}	0	0

more efficiently and to generate a higher fraction of vorticity modes in the very low Mach number limit. Consequently, the kinetic energy in the rotational ($\nabla \times \vec{v}$) modes increases relative to the kinetic energy in the compressive ($\nabla \cdot \vec{v}$) velocity modes in the very subsonic regime. This causes $E_{\text{sol}}/E_{\text{tot}}$ to grow in this limit, which then leads to an efficient SSD mechanism, thereby increasing the saturation efficiency at very low Mach numbers.

The growth rate of the dynamo depends on the Re of the plasma in the limit of very high Prandtl numbers, *Pm* >> 1 [23] and on the Rm in the limit of *Pm* << 1 [28]. In our simulations, Pm ~ 1 typically, and we will investigate how Γ depends on the Reynolds number in this regime. The Reynolds numbers of our simulations can be increased by increasing the resolution of our simulations. We study the SSD for Mach numbers, $\mathcal{M} \sim 0.01$ and ~ 0.05 with solenoidal fraction, $\zeta = 0.01$ (1%) and $\zeta = 0.001$ (0.1%) on different resolutions to understand the effect of increasing the Reynolds number on the dynamo properties.

Our results for the growth rates are shown in figure 4.11 (for $\zeta = 0.01$) and figure 4.12 (for $\zeta = 0.001$). We find that for both cases, Γ increases as we increase the resolution of our simulations and do not converge as the saturation efficiency of the SSD does (see figure 4.10). It is difficult to achieve higher resolutions in our simulations as the relevant time scale for the SSD (determined by the turn-over time (t_{ed})) is inversely proportional to the Mach number and therefore it increases in the low Mach number regime. The time step taken by the FLASH code is determined by the sound speed, c_s, which is much higher than the velocity, in the highly subsonic regime. Therefore it requires more computational resources and time to simulate the low Mach number SSD with higher resolution.

4.7   Slice plots of density and magnetic energy

The density fluctuations, which can generate seeds of vorticity in the purely compressively driven SSD, decrease with the Mach number. As we have seen earlier, the magnetic energy relies on the Mach number and the vorticity present in the plasma. To compare the behavior of the magnetic energy across simulations with different solenoidal fractions, we plot this quantity on the surface of the simulation box for a high ($\mathcal{M} \sim 0.4$) and low Mach number ($\mathcal{M} \sim 0.05$). Figure 4.13 depicts the magnitude of the magnetic energy for simulations with $\mathcal{M} \sim 0.05$ (first column) and 0.4 (second column) for $\zeta = 0$ (top row), $\zeta = 0.001$ (middle row) and $\zeta = 0.1$ (bottom row). We observe that for $\mathcal{M} \sim 0.4$, the magnetic energy appears saturated compared to the case with $\mathcal{M} \sim 0.05$ for all the

Figure 4.11: Amplification rate, Γ for solenoidal fraction $\zeta = 0.01$ in the turbulent driving with Mach number, $\mathcal{M} \sim 0.01$ and ~ 0.05. The black data points correspond to the simulations done on 256^3 grid cells and the grey data points correspond to simulations done on 512^3 grid cells.

solenoidal fractions we have considered. The value of the magnetic energy at saturation, when the Mach number is fixed, increases as the solenoidal fraction in the turbulent driving is increased.
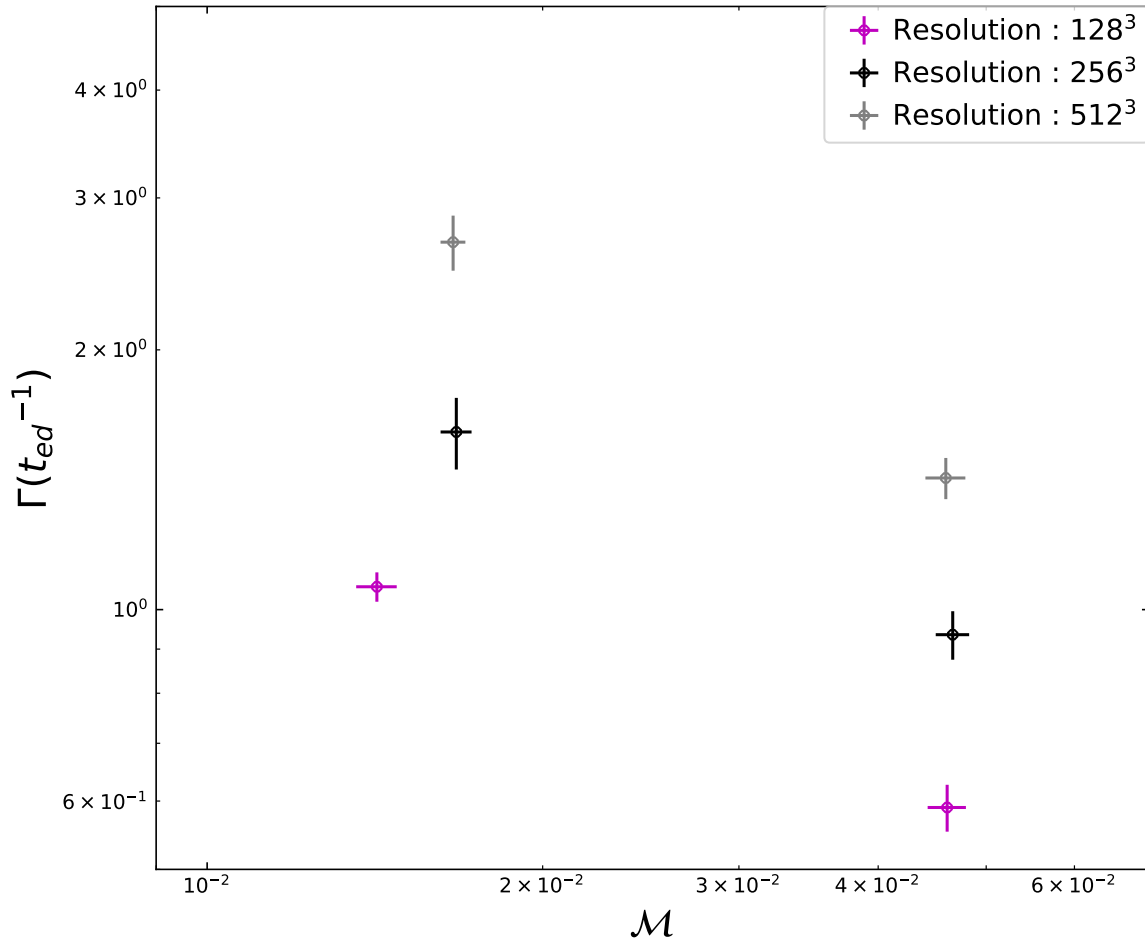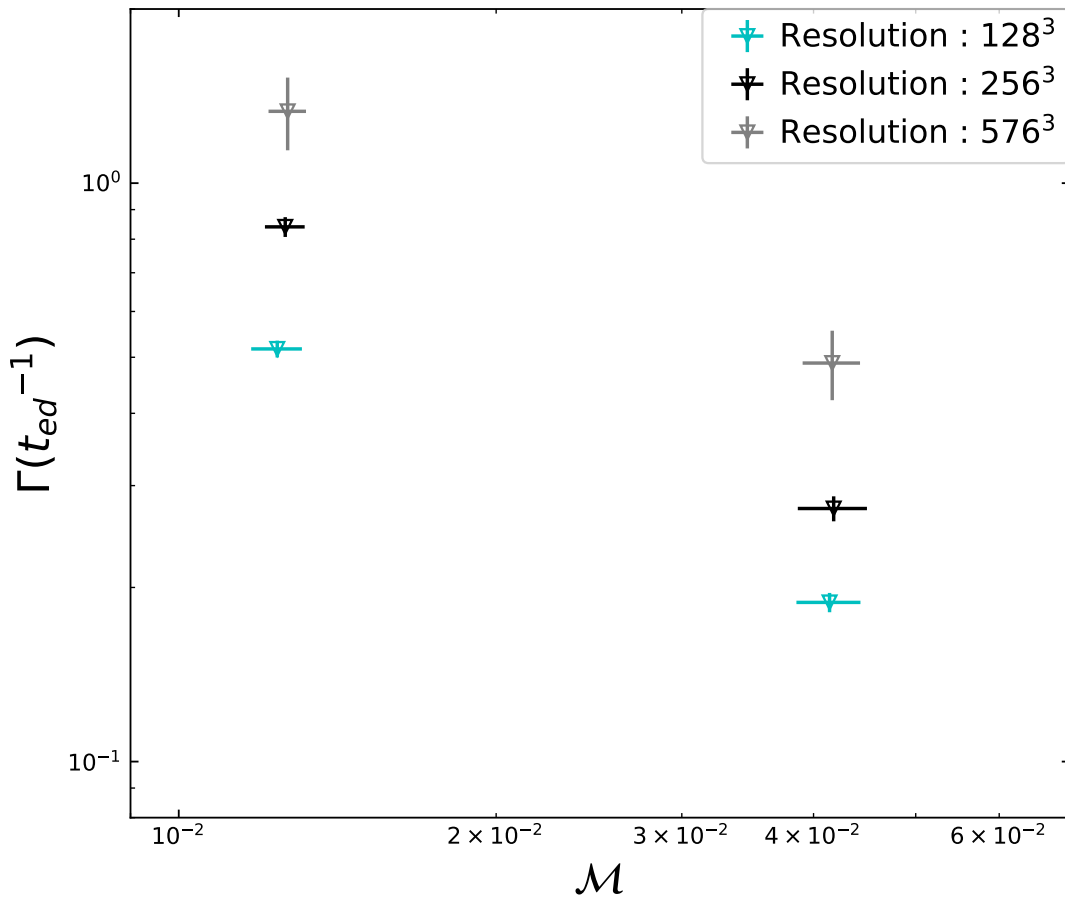
Figure 4.12: Amplification rate, Γ for solenoidal fraction $\zeta = 0.001$ in the turbulent driving with Mach number, $\mathcal{M} \sim 0.01$ and ~ 0.05. The black data points correspond to the simulations done on 256^3 grid cells and the grey data points correspond to simulations done on 576^3 grid cells.

Figure 4.14 shows the spectra of the magnetic energy and kinetic energy for our lowest Mach number simulation ($\mathcal{M} \sim 10^{-3}$) with purely compressive driving. The blue, orange and green curves show the magnetic energy spectrum at $30t_{\mathrm{ed}}$, $297t_{\mathrm{ed}}$, and $567t_{\mathrm{ed}}$ marking different times in the dynamo evolution; the initial phase, the amplification phase and the phase after the SSD has saturated. The red, purple and brown curves show the kinetic energy spectrum at $30t_{\mathrm{ed}}$, $297t_{\mathrm{ed}}$ and $567t_{\mathrm{ed}}$.

We find that the spectrum of the kinetic energy stays similar during the amplification of E_{mag} by the SSD. This is because we force the velocity field continuously in the same fashion throughout our

41
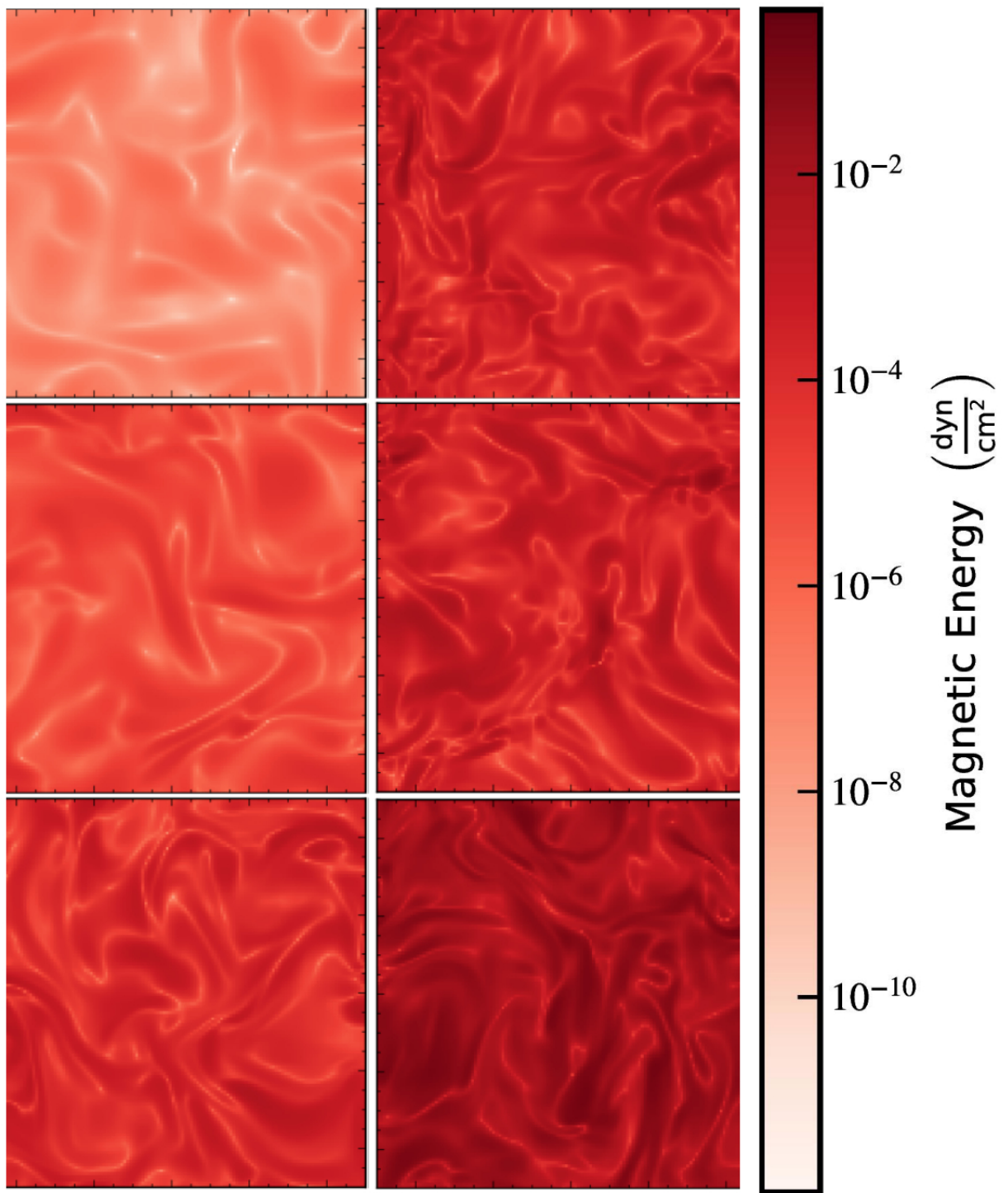
Figure 4.13: Magnetic field fluctuations for $\zeta = 0$ (top row), $\zeta = 0.001$ (middle row) and $\zeta = 0.1$ (bottom row) for Mach numbers 0.05 (first column) and 0.4 (second column) for simulations on 128^3 grid cells.
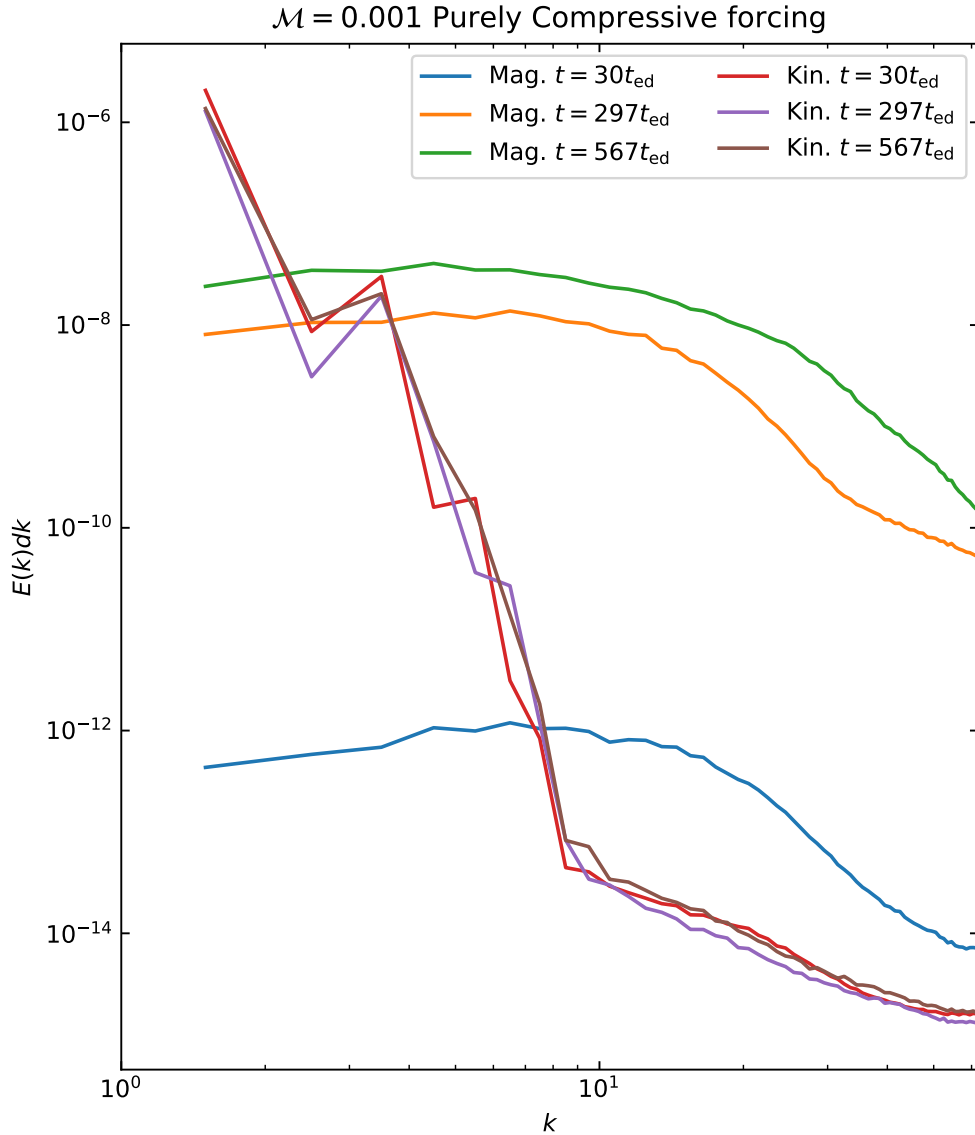
Figure 4.14: The magnetic and kinetic energy spectrum for the SSD with Mach number, $\mathcal{M} \sim 10^{-3}$ and purely compressive driving. We plot the spectra for three different phases during the dynamo action; at $30t_{\mathrm{ed}}$ during the initial phase of the dynamo action (blue curve for the magnetic energy spectrum and red curve for the kinetic energy spectrum), at $297t_{\mathrm{ed}}$, during the amplification phase (orange curve for the magnetic energy spectrum and purple curve for the kinetic energy spectrum) and at $567t_{\mathrm{ed}}$, when the magnetic energy has saturated (green curve for the magnetic energy spectrum and brown curve for the kinetic energy spectrum)
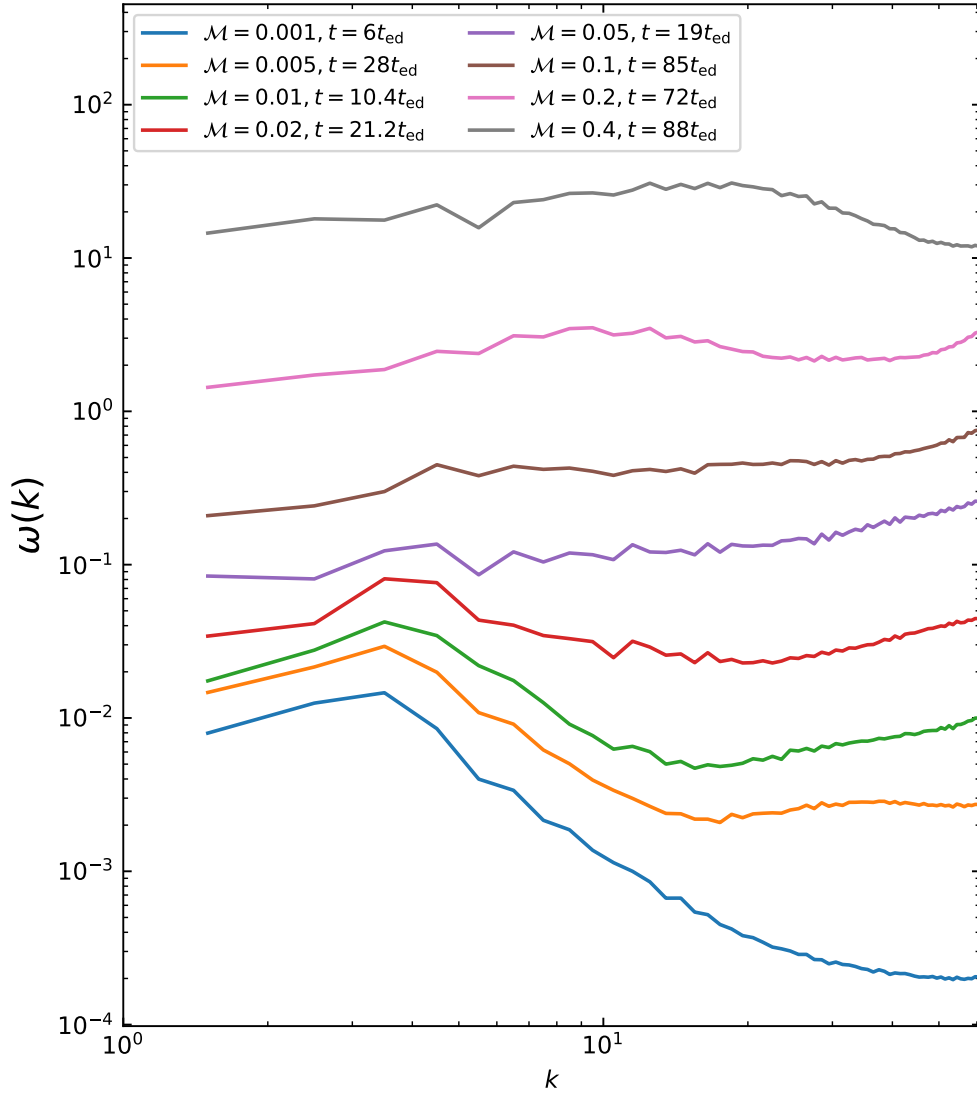
Figure 4.15: The spectra of the vorticity for the SSD with purely compressive driving for Mach numbers in the range $10^{-3} - 0.4$. The blue curve depicts the dynamo with Mach number ~ 0.001 at $6t_{\mathrm{ed}}$, the orange curve depicts the dynamo with Mach number ~ 0.005 at $28t_{\mathrm{ed}}$, the green curve depicts the dynamo with Mach number ~ 0.01 at $10.4t_{\mathrm{ed}}$, the red curve depicts the dynamo with Mach number ~ 0.02 at $21.2t_{\mathrm{ed}}$, the purple curve depicts the dynamo with Mach number ~ 0.05 at $19t_{\mathrm{ed}}$, the brown curve depicts the dynamo with Mach number ~ 0.1 at $85t_{\mathrm{ed}}$, the pink curve depicts the dynamo with Mach number ~ 0.2 at $72t_{\mathrm{ed}}$ and the grey curve depicts the dynamo with Mach number ~ 0.4 at $88t_{\mathrm{ed}}$.

44

simulations. The spectrum of the magnetic energy, however, changes dynamically with time. The SSD injects the kinetic energy at large k scales (or small length scales) into the magnetic field. We see that the power in the magnetic field grows at all scales as the dynamo amplification continues. The peak of the magnetic field spectrum remains at larger k-scales; however, we see that the energy at smaller k-scales increases as the dynamo action goes from its initial phase to the saturation phase.

Figure 4.15 shows the spectra of the vorticity for the lowest to the highest Mach numbers for the purely compressively driven SSD. The power of the vorticity at all scales decreases with the Mach number as the absolute value of the velocity decreases with the Mach number. We find that the peak of the vorticity spectra at higher Mach numbers ($\mathcal{M} \sim 0.4$) lies at larger k scales (smaller length scales) and as the Mach number decreases, the peak shifts towards smaller k scales (larger length scales). Interestingly, the inflection point for this behavior occurs at a $\mathcal{M} \sim 0.05$, which coincides with the Mach number at which E_{sol}/E_{tot} starts to rise in the highly subsonic regime (see figure 4.10).

4.8   Simulations

We assign a model name to our simulations in which "M" stands for the Mach number and "S" stands for the solenoidal fraction (ζ) in the driving field. Tabulated below, in increasing order of ζ, are the values for the Mach number ($\mathcal{M}$), solenoidal fraction in the turbulent forcing, saturation efficiency of the dynamo (($E_{mag}/E_{kin})_{sat}$), amplification rate of the magnetic energy (Γ) and the solenoidal ratio in the kinetic energy (E_{sol}/E_{tot}) for our simulations on 128^3, 256^3, 512^3 and 576^3 grid cells.

Model (Resolution 128^3)	$\mathcal{M}$	ζ	$(E_{mag}/E_{kin})_{sat}$	$\Gamma\ (t_{ed}^{-1})$	E_{sol}/E_{tot}
M0.001S0	$(9.5 \pm 1.4) \times 10^{-4}$	0	$(8.3 \pm 3.6) \times 10^{-3}$	$(5.5 \pm 0.9) \times 10^{-2}$	$(4.9 \pm 0.6) \times 10^{-2}$
M0.005S0	$(3.9 \pm 0.3) \times 10^{-3}$	0	$(2.4 \pm 0.8) \times 10^{-3}$	$(2.1 \pm 0.2) \times 10^{-2}$	$(1.1 \pm 0.2) \times 10^{-2}$
M0.01S0	$(1.0 \pm 0.1) \times 10^{-2}$	0	$(1.3 \pm 0.2) \times 10^{-3}$	$(4.8 \pm 0.3) \times 10^{-2}$	$(9.7 \pm 1.7) \times 10^{-3}$
M0.02S0	$(2.0 \pm 0.2) \times 10^{-2}$	0	$(2.8 \pm 0.6) \times 10^{-4}$	$(2.7 \pm 0.2) \times 10^{-2}$	$(3.1 \pm 0.5) \times 10^{-3}$
M0.05S0	$(4.8 \pm 0.4) \times 10^{-2}$	0	$(2.3 \pm 0.5) \times 10^{-4}$	$(1.1 \pm 0.1) \times 10^{-2}$	$(1.5 \pm 0.3) \times 10^{-3}$
M0.1S0	$(9.7 \pm 0.9) \times 10^{-2}$	0	$(5.7 \pm 1.7) \times 10^{-4}$	$(2.3 \pm 0.2) \times 10^{-2}$	$(4.8 \pm 0.8) \times 10^{-3}$
M0.2S0	$(1.9 \pm 0.2) \times 10^{-1}$	0	$(3.7 \pm 0.9) \times 10^{-3}$	$(8.5 \pm 0.4) \times 10^{-2}$	$(3.3 \pm 0.7) \times 10^{-2}$
M0.4S0	$(4.3 \pm 0.3) \times 10^{-1}$	0	$(1.6 \pm 0.3) \times 10^{-2}$	$(2.4 \pm 0.1) \times 10^{-1}$	$(1.1 \pm 0.1) \times 10^{-1}$
M0.001S0.0001	$(1.0 \pm 0.1) \times 10^{-3}$	0.0001	$(7.6 \pm 2.3) \times 10^{-2}$	$(2.2 \pm 0.2) \times 10^{-1}$	$(2.7 \pm 0.1) \times 10^{-1}$
M0.005S0.0001	$(4.6 \pm 0.4) \times 10^{-3}$	0.0001	$(1.2 \pm 0.4) \times 10^{-2}$	$(9.2 \pm 1.2) \times 10^{-2}$	$(5.5 \pm 0.9) \times 10^{-2}$
M0.01S0.0001	$(8.0 \pm 0.6) \times 10^{-3}$	0.0001	$(6.6 \pm 1.0) \times 10^{-3}$	$(6.0 \pm 0.3) \times 10^{-2}$	$(2.0 \pm 0.4) \times 10^{-2}$
M0.02S0.0001	$(2.1 \pm 0.2) \times 10^{-2}$	0.0001	$(2.8 \pm 0.4) \times 10^{-3}$	$(6.6 \pm 0.5) \times 10^{-2}$	$(1.4 \pm 0.2) \times 10^{-2}$
M0.05S0.0001	$(4.6 \pm 0.4) \times 10^{-2}$	0.0001	$(1.1 \pm 0.2) \times 10^{-3}$	$(3.1 \pm 0.3) \times 10^{-2}$	$(4.4 \pm 1.0) \times 10^{-3}$
M0.1S0.0001	$(1.3 \pm 0.1) \times 10^{-1}$	0.0001	$(1.9 \pm 0.6) \times 10^{-3}$	$(6.4 \pm 0.5) \times 10^{-2}$	$(1.0 \pm 0.1) \times 10^{-2}$
M0.2S0.0001	$(1.9 \pm 0.2) \times 10^{-1}$	0.0001	$(4.7 \pm 1.1) \times 10^{-3}$	$(8.0 \pm 0.4) \times 10^{-2}$	$(3.1 \pm 0.3) \times 10^{-2}$
M0.4S0.0001	$(4.4 \pm 0.4) \times 10^{-1}$	0.0001	$(1.7 \pm 0.4) \times 10^{-2}$	$(2.5 \pm 0.1) \times 10^{-1}$	$(9.1 \pm 1.8) \times 10^{-2}$
M0.001S0.001	$(1.1 \pm 0.1) \times 10^{-3}$	0.001	$(3.5 \pm 0.5) \times 10^{-1}$	$(4.4 \pm 0.3) \times 10^{-1}$	$(8.8 \pm 0.3) \times 10^{-1}$
M0.005S0.001	$(5.7 \pm 0.2) \times 10^{-3}$	0.001	$(1.7 \pm 0.3) \times 10^{-1}$	$(4.8 \pm 0.2) \times 10^{-1}$	$(4.0 \pm 0.7) \times 10^{-1}$
M0.01S0.001	$(1.2 \pm 0.1) \times 10^{-2}$	0.001	$(1.0 \pm 0.2) \times 10^{-1}$	$(5.2 \pm 0.2) \times 10^{-1}$	$(2.6 \pm 0.7) \times 10^{-1}$
M0.02S0.001	$(2.3 \pm 0.1) \times 10^{-2}$	0.001	$(5.9 \pm 1.0) \times 10^{-2}$	$(3.5 \pm 0.1) \times 10^{-1}$	$(1.1 \pm 0.0) \times 10^{-1}$
M0.05S0.001	$(4.1 \pm 0.3) \times 10^{-2}$	0.001	$(2.8 \pm 0.5) \times 10^{-2}$	$(1.9 \pm 0.1) \times 10^{-1}$	$(6.5 \pm 0.5) \times 10^{-2}$
M0.1S0.001	$(9.9 \pm 0.9) \times 10^{-2}$	0.001	$(1.2 \pm 0.2) \times 10^{-2}$	$(1.5 \pm 0.1) \times 10^{-1}$	$(4.0 \pm 0.6) \times 10^{-2}$
M0.2S0.001	$(1.8 \pm 0.2) \times 10^{-1}$	0.001	$(6.6 \pm 1.5) \times 10^{-3}$	$(9.2 \pm 0.5) \times 10^{-2}$	$(3.5 \pm 0.6) \times 10^{-2}$
M0.4S0.001	$(3.9 \pm 0.3) \times 10^{-1}$	0.001	$(1.4 \pm 0.3) \times 10^{-2}$	$(1.7 \pm 0.1) \times 10^{-1}$	$(1.0 \pm 0.1) \times 10^{-1}$
M0.001S0.01	$(1.1 \pm 0.2) \times 10^{-3}$	0.01	$(6.1 \pm 1.3) \times 10^{-1}$	$(5.8 \pm 0.5) \times 10^{-1}$	$(1.0 \pm 0.0) \times 10^{+0}$
M0.005S0.01	$(5.1 \pm 0.2) \times 10^{-3}$	0.01	$(4.3 \pm 1.0) \times 10^{-1}$	$(5.5 \pm 0.3) \times 10^{-1}$	$(9.6 \pm 0.1) \times 10^{-1}$
M0.01S0.01	$(1.4 \pm 0.1) \times 10^{-2}$	0.01	$(5.0 \pm 1.0) \times 10^{-1}$	$(1.1 \pm 0.0) \times 10^{+0}$	$(7.8 \pm 0.2) \times 10^{-1}$
M0.02S0.01	$(2.2 \pm 0.1) \times 10^{-2}$	0.01	$(3.5 \pm 0.6) \times 10^{-1}$	$(8.6 \pm 0.5) \times 10^{-1}$	$(6.7 \pm 0.8) \times 10^{-1}$
M0.05S0.01	$(4.6 \pm 0.2) \times 10^{-2}$	0.01	$(2.4 \pm 0.3) \times 10^{-1}$	$(5.9 \pm 0.4) \times 10^{-1}$	$(5.2 \pm 0.1) \times 10^{-1}$
M0.1S0.01	$(9.3 \pm 0.6) \times 10^{-2}$	0.01	$(1.6 \pm 0.3) \times 10^{-1}$	$(5.7 \pm 0.3) \times 10^{-1}$	$(3.9 \pm 0.6) \times 10^{-1}$
M0.2S0.01	$(2.1 \pm 0.2) \times 10^{-1}$	0.01	$(8.3 \pm 1.6) \times 10^{-2}$	$(5.1 \pm 0.1) \times 10^{-1}$	$(1.9 \pm 0.3) \times 10^{-1}$
M0.4S0.01	$(3.8 \pm 0.3) \times 10^{-1}$	0.01	$(3.4 \pm 0.7) \times 10^{-2}$	$(2.8 \pm 0.3) \times 10^{-1}$	$(1.4 \pm 0.1) \times 10^{-1}$
M0.001S0.1	$(1.2 \pm 0.1) \times 10^{-3}$	0.1	$(5.4 \pm 1.0) \times 10^{-1}$	$(5.2 \pm 0.6) \times 10^{-1}$	$(1.0 \pm 0.0) \times 10^{+0}$
M0.005S0.1	$(4.4 \pm 0.3) \times 10^{-3}$	0.1	$(6.4 \pm 1.9) \times 10^{-1}$	$(6.1 \pm 0.4) \times 10^{-1}$	$(1.0 \pm 0.0) \times 10^{+0}$
M0.01S0.1	$(9.3 \pm 0.5) \times 10^{-3}$	0.1	$(5.4 \pm 1.0) \times 10^{-1}$	$(7.6 \pm 0.2) \times 10^{-1}$	$(1.0 \pm 0.0) \times 10^{+0}$
M0.02S0.1	$(1.9 \pm 0.1) \times 10^{-2}$	0.1	$(5.3 \pm 1.1) \times 10^{-1}$	$(7.5 \pm 0.2) \times 10^{-1}$	$(9.8 \pm 0.1) \times 10^{-1}$
M0.05S0.1	$(4.9 \pm 0.2) \times 10^{-2}$	0.1	$(4.7 \pm 0.8) \times 10^{-1}$	$(8.9 \pm 0.6) \times 10^{-1}$	$(9.2 \pm 0.1) \times 10^{-1}$
M0.1S0.1	$(1.0 \pm 0.0) \times 10^{-1}$	0.1	$(4.2 \pm 0.7) \times 10^{-1}$	$(9.1 \pm 0.4) \times 10^{-1}$	$(8.9 \pm 0.2) \times 10^{-1}$
M0.2S0.1	$(2.1 \pm 0.1) \times 10^{-1}$	0.1	$(3.4 \pm 0.6) \times 10^{-1}$	$(9.5 \pm 0.4) \times 10^{-1}$	$(8.2 \pm 0.3) \times 10^{-1}$
M0.4S0.1	$(4.3 \pm 0.1) \times 10^{-1}$	0.1	$(2.5 \pm 0.4) \times 10^{-1}$	$(8.6 \pm 0.5) \times 10^{-1}$	$(7.3 \pm 0.4) \times 10^{-1}$

4.9   Applications

In this section, we discuss the applications of the SSD in the low Mach number regime to the primordial magnetic fields and estimate values for the intergalactic magnetic fields from our results. We also discuss the applications of our study to the stellar corona and the galactic halo.

Model (Resolution 256^3)	$\mathcal{M}$	ζ	$(E_{mag}/E_{kin})_{sat}$	Γ (t_{ed}^{-1})	E_{sol}/E_{tot}
M0.005S0.001	$(6.3 \pm 0.2) \times 10^{-3}$	0.001	$(2.0 \pm 0.2) \times 10^{-1}$	$(8.8 \pm 0.7) \times 10^{-1}$	$(6.0 \pm 0.4) \times 10^{-1}$
M0.01S0.001	$(1.3 \pm 0.1) \times 10^{-2}$	0.001	$(1.2 \pm 0.2) \times 10^{-1}$	$(8.4 \pm 0.3) \times 10^{-1}$	$(3.8 \pm 0.2) \times 10^{-1}$
M0.02S0.001	$(2.4 \pm 0.1) \times 10^{-2}$	0.001	$(7.3 \pm 1.1) \times 10^{-2}$	$(5.7 \pm 0.3) \times 10^{-1}$	$(2.0 \pm 0.4) \times 10^{-1}$
M0.05S0.001	$(4.2 \pm 0.3) \times 10^{-2}$	0.001	$(3.2 \pm 0.5) \times 10^{-2}$	$(2.7 \pm 0.1) \times 10^{-1}$	$(8.5 \pm 1.1) \times 10^{-2}$
M0.1S0.001	$(9.8 \pm 0.8) \times 10^{-2}$	0.001	$(1.5 \pm 0.3) \times 10^{-2}$	$(2.5 \pm 0.1) \times 10^{-1}$	$(5.0 \pm 0.2) \times 10^{-2}$
M0.005S0.01	$(5.4 \pm 0.2) \times 10^{-3}$	0.01	$(4.9 \pm 0.5) \times 10^{-1}$	$(1.0 \pm 0.0) \times 10^{+0}$	$(9.9 \pm 0.0) \times 10^{-1}$
M0.01S0.01	$(1.7 \pm 0.1) \times 10^{-2}$	0.01	$(4.1 \pm 0.4) \times 10^{-1}$	$(1.6 \pm 0.1) \times 10^{+0}$	$(8.5 \pm 0.6) \times 10^{-1}$
M0.02S0.01	$(2.6 \pm 0.1) \times 10^{-2}$	0.01	$(3.4 \pm 0.4) \times 10^{-1}$	$(1.4 \pm 0.1) \times 10^{+0}$	$(6.8 \pm 0.6) \times 10^{-1}$
M0.05S0.01	$(4.7 \pm 0.2) \times 10^{-2}$	0.01	$(2.4 \pm 0.4) \times 10^{-1}$	$(9.4 \pm 0.6) \times 10^{-1}$	$(5.0 \pm 0.0) \times 10^{-1}$
M0.1S0.01	$(9.4 \pm 0.5) \times 10^{-2}$	0.01	$(1.9 \pm 0.3) \times 10^{-1}$	$(8.5 \pm 0.6) \times 10^{-1}$	$(3.3 \pm 0.3) \times 10^{-1}$
Model (Resolution 512^3)					
M0.01S0.01	$(1.7 \pm 0.0) \times 10^{-2}$	0.01	$(5.7 \pm 0.4) \times 10^{-1}$	$(2.7 \pm 0.2) \times 10^{+0}$	$(8.8 \pm 0.1) \times 10^{-1}$
M0.05S0.01	$(4.6 \pm 0.2) \times 10^{-2}$	0.01	$(1.8 \pm 0.4) \times 10^{-1}$	$(1.4 \pm 0.1) \times 10^{+0}$	$(5.7 \pm 0.3) \times 10^{-1}$
Model (Resolution 576^3)					
M0.01S0.001	$(1.3 \pm 0.1) \times 10^{-2}$	0.001	$(9.5 \pm 1.2) \times 10^{-2}$	$(1.3 \pm 0.2) \times 10^{+0}$	$(3.1 \pm 0.1) \times 10^{-1}$
M0.05S0.001	$(4.2 \pm 0.3) \times 10^{-2}$	0.001	$(2.8 \pm 0.5) \times 10^{-2}$	$(4.9 \pm 0.7) \times 10^{-1}$	$(8.1 \pm 1.1) \times 10^{-2}$

Table 4.5: Table of all simulations with their corresponding Mach number ($\mathcal{M}$), solenoidal fraction (ζ) in the turbulent driving, saturation efficiency of the dynamo (($E_{mag}/E_{kin})_{sat}$), amplification rate of the magnetic energy (Γ) and the solenoidal ratio in the kinetic energy (E_{sol}/E_{tot})

4.9.1 Primordial magnetic fields

Magnetic fields are unavoidably created in the primordial Universe [15] and can act as a seed for the SSD. [17] show that turbulence can be established in the early Universe between the electroweak epoch and neutrino decoupling ($T = 0.2$–$100\,\mathrm{GeV}$). They further describe two mechanisms for driving the turbulence in this early evolution of the Universe: 1) through velocity fluctuations generated through primordial density perturbations (PDP), and 2) phase transitions, which may occur in this epoch. In the former case, the velocity fluctuations arise due to acceleration by the gravitational potential generated due to PDP and therefore are longitudinal or compressive velocity modes. They would also be driven continuously, as is the case in our simulations.

Well developed turbulence, together with the high magnetic Reynolds numbers and Pm in the early Universe, provides optimal conditions for the SSD to function. This dynamo is expected to have worked in very subsonic conditions, $\mathcal{M} \sim 10^{-4}$.

Now, we will apply our results for the SSD in the subsonic regime to the early Universe. At $\mathcal{M} \sim 10^{-3}$ we report the saturation efficiency to be $\sim 8.3 \times 10^{-3}$. We also find that as the Mach number is decreased in this regime, the saturation efficiency increases. Taking the value of the saturation efficiency at $\mathcal{M} \sim 10^{-3}$ to be a lower bound for the early-Universe dynamo, we predict the

generation of magnetic fields with strengths $\gtrsim 9.1 \times 10^{-17}$ Gauss on scales of $\lambda_c \sim 0.1$ pc through the SSD action driven by primordial density perturbations. If the SSD is driven by first-order phase transitions, we predict that the dynamo generates much higher magnetic field strengths of $\gtrsim 9.1 \times 10^{-14}$ Gauss on scales of $\lambda_c \sim 100$ pc [17]. We note that these values are lower limits, as the magnetic field generated increases with the saturation efficiency, which is likely to be appreciably greater in the primordial Universe.

The conservative estimates of the lower bounds on the IGMF from blazar γ-ray observations are 10^{-17}–10^{-14} Gauss on scales of 0.1 pc and 10^{-19}–10^{-15} Gauss on scales of 100 pc [7, 8]. The SSD mechanism driven by first-order phase transitions in the primordial Universe can, therefore, explain the lower-limit on the IGMFs on scales of ~ 100 pc. The dynamo mechanism driven by PDPs can produce appreciable magnetic fields at shorter scales of 0.1 pc comparable to the lower bounds on the IGMF at these scales. This raises the interesting possibility of explaining the IGMF lower limits on these scales, without invoking beyond the standard model (BSM) physics, i.e., without requiring a first-order phase transition.

These primordial fields can act as seeds for galactic dynamos and may influence the formation of the first stars [35, 36]. The Reynolds numbers in the early Universe are orders of magnitude higher than what we achieve. In this limit, the growth rate increases with the Reynolds number as $\Gamma \propto Re^{1/2}$ [23]. Therefore, the growth rate of the early-Universe dynamo will be much higher than what is predicted from our simulations [22].

4.9.2 Stellar Coronae

Another possible astrophysical application of low Mach number MHD turbulence and the SSD could be in stellar coronae. For the solar corona, at heights $h \sim 2 - 5 R_\odot$ above the photosphere, the sonic and Alfvénic Mach numbers are both typically $\sim 10^{-2}$ [37, 38]. Here the Rm is very high $\sim 10^8 - 10^{12}$, and the kinetic Mach number is also high enough ($Re \sim 10^4$) [39] for turbulence to develop. Although the plasma beta is initially low $\beta < 1$ at $h < 0.2 R_\odot$ it acquires large values above unity $\beta \sim 10$ [40] in this height range $h \sim 2 - 5 R_\odot$ that describes the outer corona and the solar wind accelerating region. Coronal observations also indicate a continuous forcing of the velocity fields with plasma velocities of $v_{rms} \sim 1$ km s^{-1} (outside of coronal holes and the emerging fast solar wind) along with fine-grained structure. In such a system, we could expect a low Mach number SSD to develop and amplify magnetic energy. Interestingly, the magnetic field strengths, over an

active region, in the outer corona at $h \sim 2R_\odot$ are $B \sim 10^{-1}$ G [41], whereas an extrapolation of the stretched potential field model yields $B \sim 10^{-3}$ G. We note that an MHD description of turbulence would be valid only on scales significantly larger than the particle mean free path ($\sim 10^3$ km at these heights [42]).

4.9.3   Hot Interstellar Medium in the Galactic Halo

Our results may also be relevant in the growth of the Galactic halo (corona) magnetic fields of strengths $B \sim 1\mu$G, especially at large radii $R \gtrsim 5$ kpc [43, 44, 45, 46, 47, 48]. In these regions, the hot interstellar medium (HIM) typically has $T \simeq 10^6$ K, $\mathcal{M} \sim 10^{-1}$, $\mathcal{M}_{\mathcal{A}} \sim 10^{-1}$, $Re \sim 10^2$, Rm $\sim 10^{22}$ and a magnetic Prandtl number Pm $\sim 10^{20}$ with plasma beta $\beta \gtrsim 3$ [49, 50]. Thus it appears plausible that a low-Mach SSD could have played a role in the development of Galactic halo fields. We caution that the baryonic halo HIM, with weaker kinetic turbulence and containing wakes of high-velocity clouds would not be continuously forced in the same manner as our simulations. Interestingly, the mean-field SSD model for halo fields [51] appears to be disfavoured by simulations [52].

Chapter 5

Conclusion and Outlook

We study the properties of the SSD for a wide range of Mach numbers in the highly subsonic limit. We investigate the amplification rate and the saturation efficiency of the SSD for Mach numbers between 0.4 and 10^{-3} by performing numerical simulations on a periodic computational grid with 128^3, 256^3, 512^3 and 576^3 grid cells. Previous studies by [21] have investigated the properties of the SSD driven purely by rotational and longitudinal driving modes for Mach numbers in the range $\sim 0.02 - 20$ and $\sim 0.1 - 20$ respectively. We extend the study of the small scale dynamo driven solely by longitudinal modes further into the subsonic regime, up to a Mach number of $\sim 10^{-3}$. In this case, we find that the saturation efficiency and the amplification rate of the dynamo decrease until $\mathcal{M} \sim 0.05$ and then begin to increase in the highly subsonic regime. Our study explores the previously unexplored subsonic limit and along with the earlier study by [21], we have the Mach number dependence of the properties of the SSD in the sub-sonic, trans-sonic and the super sonic regime.

Besides the case when the dynamo is driven by compressive or longitudinal driving, we also study the a wide range of forcing conditions. We change the solenoidal component in the forcing field by changing the projection parameter ζ to 0.1 (10%), 0.01 (1%), 0.001 (0.1%) and 0.0001 (0.01%). We find that when $\zeta = 0.1$, the saturation efficiency of the SSD is similar to what is obtained for a purely rotational forcing of the driving field ($\zeta = 1$) or incompressible turbulence. In this case, we find that the solenoidal fraction in the kinetic energy, $E_{\text{sol}}/E_{\text{tot}}$, is close to ~ 1. For the cases of the SSD with solenoidal fraction of 1% and 0.1% in the turbulent driving, we find that the $E_{\text{sol}}/E_{\text{tot}}$ approaches 1 in the highly subsonic limit thereby increasing the saturation efficiency

in this limit. When the solenoidal fraction in the turbulent driving is set to 0.01%, we find similar behaviour as the case with purely compressive driving of the turbulence. The solenoidal fraction in the kinetic energy and the saturation efficiency of the SSD decreases until a Mach number ~ 0.05 and then increase as the Mach number decreases. Our results are summarised in Figure 4.10. We also fit models to the saturation efficiencies and $E_{\rm sol}/E_{\rm tot}$ as a function of the Mach number for our results. The growth rate of the SSD is correlated to $E_{\rm sol}/E_{\rm tot}$ and we find that as $E_{\rm sol}/E_{\rm tot}$ increases in the very subsonic limit the growth rates of the dynamo increase as well for all the models we have studied. The growth rate of the dynamo is a function of the Reynolds numbers which depends on the resolution of our simulations. We investigate the vorticity generated in the plasma to understand the growth of $E_{\rm sol}/E_{\rm tot}$ in the highly subsonic regime.

The $\gamma-$ray observations of TeV blazars estimate the lower bounds on the intergalactic magnetic fields to be 10^{-17}–10^{-14} Gauss on scales of 0.1 pc and 10^{-19}–10^{-15} Gauss on scales of 100 pc [7, 8]. [17] proposed that a SSD in the early universe can amplify magnetic fields exponentially. They proposed two mechanisms that can generate turbulence in the early universe; through velocity fluctuations driven by primordial density perturbations and through first order phase transitions that may occur in the early universe. The turbulence driven by the primordial density perturbations is compressive in nature and the Mach numbers in the early universe are expected to be $10^{-5} - 10^{-4}$.

Using our results on the SSD in the low Mach number regime, we predict the generation of magnetic fields with strengths $\gtrsim 9.1 \times 10^{-17}$ Gauss on scales of $\lambda_c \sim 0.1$ pc through the SSD action driven by primordial density perturbations. If the SSD is driven by first-order phase transitions, we predict that the dynamo generates much higher magnetic field strengths of $\gtrsim 9.1 \times 10^{-14}$ Gauss on scales of $\lambda_c \sim 100$ pc [17]. The values we predict are lower limits, as the magnetic field generated increases with the saturation efficiency, which is likely to be appreciably greater in the early Universe. The saturation efficiency and the amplification rate of the dynamo is dependent on Pm of the plasma which is much higher in the early universe ($10^2 - 10^{12}$) compared to our simulations, where Pm ~ 1. We find that the value of the saturation efficiency converges as the resolution of the simulations is increased. The growth rate, however, increases a with the resolution. The Reynolds numbers in the early universe are much higher than what is obtained in our simulations and in this case the growth rate $\Gamma \propto Re^{1/2}$ [23]. Therefore, the dynamo growth rates in the early universe are very high and can lead to saturation of magnetic energy by the SSD action on small time scales.

Our results can therefore explain the lower bound on the intergalactic magnetic fields on scales of 0.1 pc and 100 pc. At smaller scales of 0.1 pc, a dynamo driven by primordial density perturbations,

without requiring a first order phase transition in the early universe, can lead to magnetic field strengths on these scales inferred for the $\gamma-$ray observations. The low Mach number dynamo can act in the stellar corona where the kinetic Reynolds numbers and magnetic Reynolds numbers are high. It can also be relevant in the growth of magnetic fields in the galactic corona.

The small-scale turbulent dynamo is an efficient process for magnetic field amplification and has many applications in astrophysical settings. It is therefore important to understand its properties in different parameter regimes. We explore the SSD in the previously unexplored highly subsonic regime for a wide range of forcing conditions. We apply our results to understand the primordial magnetic field strengths. Our results are more general and can be relevant to studies on magnetohydrodynamic turbulence. They may also have further applications for studies in astrophysics and cosmology.

Bibliography

[1] Andrii Neronov and Ievgen Vovk. Evidence for Strong Extragalactic Magnetic Fields from Fermi Observations of TeV Blazars. *Science*, 328(5974):73, Apr 2010.

[2] F. Tavecchio, G. Ghisellini, L. Foschini, G. Bonnoli, G. Ghirlanda, and P. Coppi. The intergalactic magnetic field constrained by Fermi/Large Area Telescope observations of the TeV blazar 1ES0229+200. *Mon. Not. R. Astron. Soc.* , 406(1):L70–L74, Jul 2010.

[3] K. Dolag, M. Kachelriess, S. Ostapchenko, and R. Tomàs. Lower Limit on the Strength and Filling Factor of Extragalactic Magnetic Fields. *Astrophys. J. L.* , 727(1):L4, Jan 2011.

[4] A. M. Taylor, I. Vovk, and A. Neronov. Extragalactic magnetic fields constraints from simultaneous GeV-TeV observations of blazars. *Astron. Astrophys.* , 529:A144, May 2011.

[5] Ie. Vovk, A. M. Taylor, D. Semikoz, and A. Neronov. Fermi/LAT Observations of 1ES 0229+200: Implications for Extragalactic Magnetic Fields and Background Light. *Astrophys. J. L.* , 747(1):L14, Mar 2012.

[6] Keitaro Takahashi, Masaki Mori, Kiyotomo Ichiki, Susumu Inoue, and Hajime Takami. Lower Bounds on Magnetic Fields in Intergalactic Voids from Long-term GeV-TeV Light Curves of the Blazar Mrk 421. *Astrophys. J. L.* , 771(2):L42, Jul 2013.

[7] Justin D. Finke, Luis C. Reyes, Markos Georganopoulos, Kaeleigh Reynolds, Marco Ajello, Stephen J. Fegan, and Kevin McCann. Constraints on the Intergalactic Magnetic Field with Gamma-Ray Observations of Blazars. , 814(1):20, Nov 2015.

[8] M. Ackermann et al. The Search for Spatial Extension in High-latitude Sources Detected by the Fermi Large Area Telescope. *Astrophys. J. S.* , 237(2):32, Aug 2018. The *Fermi*-LAT Collaboration.

[9] Avery E. Broderick, Philip Chang, and Christoph Pfrommer. The Cosmological Impact of Luminous TeV Blazars. I. Implications of Plasma Instabilities for the Intergalactic Magnetic Field and Extragalactic Gamma-Ray Background. , 752(1):22, Jun 2012.

[10] Rafael Alves Batista, Andrey Saveliev, and Elisabete M. de Gouveia Dal Pino. The impact of plasma instabilities on the spectra of TeV blazars. *Mon. Not. R. Astron. Soc.* , 489(3):3836–3849, Nov 2019.

[11] Dahai Yan, Jianeng Zhou, Pengfei Zhang, Qianqian Zhu, and Jiancheng Wang. Impact of Plasma Instability on Constraint of the Intergalactic Magnetic Field. , 870(1):17, Jan 2019.

[12] Kandaswamy Subramanian. The origin, evolution and signatures of primordial magnetic fields. *Reports on Progress in Physics*, 79(7):076901, Jul 2016.

[13] Günter Sigl, Angela V. Olinto, and Karsten Jedamzik. Primordial magnetic fields from cosmological first order phase transitions. , 55(8):4582–4590, Apr 1997.

[14] Michael S. Turner and Lawrence M. Widrow. Inflation-produced, large-scale magnetic fields. , 37(10):2743–2754, May 1988.

[15] E. R. Harrison. Generation of magnetic fields in the radiation ERA. *Mon. Not. R. Astron. Soc.* , 147:279, Jan 1970.

[16] S. Matarrese, S. Mollerach, A. Notari, and A. Riotto. Large-scale magnetic fields from density perturbations. , 71(4):043502, Feb 2005.

[17] Jacques M. Wagstaff, Robi Banerjee, Dominik Schleicher, and Günter Sigl. Magnetic field amplification by the small-scale dynamo in the early Universe. , 89(10):103001, May 2014.

[18] A. P. Kazantsev. Enhancement of a Magnetic Field by a Conducting Fluid. *Soviet Journal of Experimental and Theoretical Physics*, 26:1031, May 1968.

[19] Axel Brandenburg and Kandaswamy Subramanian. Astrophysical magnetic fields and nonlinear dynamo theory. *Phys. Rep.* , 417(1-4):1–209, Oct 2005.

[20] AA Ruzmaikin, AM Shukurov, and DD Sokoloff. *Magnetic Fields of Galaxies*. Academic Press, Dordrecht, 1988.

[21] C. Federrath, G. Chabrier, J. Schober, R. Banerjee, R. S. Klessen, and D. R. G. Schleicher. Mach Number Dependence of Turbulent Magnetic Field Amplification: Solenoidal versus Compressive Flows. , 107(11):114504, Sep 2011.

[22] Christoph Federrath, Jennifer Schober, Stefano Bovino, and Dominik R. G. Schleicher. The Turbulent Dynamo in Highly Compressible Supersonic Plasmas. *Astrophys. J. L.* , 797(2):L19, Dec 2014.

[23] Jennifer Schober, Dominik Schleicher, Christoph Federrath, Ralf Klessen, and Robi Banerjee. Magnetic field amplification by small-scale dynamo action: Dependence on turbulence models and Reynolds and Prandtl numbers. , 85(2):026303, Feb 2012.

[24] J. Schober, D. R. G. Schleicher, C. Federrath, S. Bovino, and R. S. Klessen. Saturation of the turbulent dynamo. , 92(2):023010, Aug 2015.

[25] C. Federrath, J. Roman-Duval, R. S. Klessen, W. Schmidt, and M. M. Mac Low. Comparing the statistics of interstellar turbulence in simulations and observations. Solenoidal versus compressive turbulence forcing. *Astron. Astrophys.* , 512:A81, Mar 2010.

[26] Anvar Shukurov and Kandaswamy Subramanian. Notes on magnetohydrodynamics.

[27] Arnab Rai Choudhuri. *The Physics of Fluids and Plasmas: An Introduction for Astrophysicists*. Cambridge University Press, 1998.

[28] Jennifer Schober, Dominik Schleicher, Stefano Bovino, and Ralf S. Klessen. Small-scale dynamo at low magnetic Prandtl numbers. , 86(6):066412, Dec 2012.

[29] Sharanya Sur, D. R. G. Schleicher, Robi Banerjee, Christoph Federrath, and Ralf S. Klessen. The Generation of Strong Magnetic Fields During the Formation of the First Stars. *Astrophys. J. L.* , 721(2):L134–L138, Oct 2010.

[30] Christoph Federrath, Sharanya Sur, Dominik R. G. Schleicher, Robi Banerjee, and Ralf S. Klessen. A New Jeans Resolution Criterion for (M)HD Simulations of Self-gravitating Gas: Application to Magnetic Field Amplification by Gravity-driven Turbulence. , 731(1):62, Apr 2011.

[31] Jennifer Schober, Dominik Schleicher, Christoph Federrath, Simon Glover, Ralf S. Klessen, and Robi Banerjee. The Small-scale Dynamo and Non-ideal Magnetohydrodynamics in Primordial Star Formation. , 754(2):99, Aug 2012.

[32] B. Fryxell, K. Olson, P. Ricker, F. X. Timmes, M. Zingale, D. Q. Lamb, P. MacNeice, R. Rosner, J. W. Truran, and H. Tufo. FLASH: An Adaptive Mesh Hydrodynamics Code for Modeling Astrophysical Thermonuclear Flashes. *Astrophys. J. S.* , 131(1):273–334, Nov 2000.

[33] Uriel Frisch. *Turbulence*. 1995.

[34] Antony J. Mee and Axel Brandenburg. Turbulence from localized random expansion waves. *Mon. Not. R. Astron. Soc.* , 370(1):415–419, Jul 2006.

[35] Lawrence M. Widrow. Origin of galactic and extragalactic magnetic fields. *Reviews of Modern Physics*, 74(3):775–823, Jan 2002.

[36] Christoph Federrath. The turbulent formation of stars. *Physics Today*, 71(6):38–42, Jun 2018.

[37] Markus J. Aschwanden. *Physics of the Solar Corona. An Introduction*. Praxis Publishing Ltd, 2004.

[38] Dieter Biskamp. *Magnetohydrodynamic Turbulence*. Cambridge University Press, 2003.

[39] Alan W. Hood and David W. Hughes. Solar magnetic fields. *Physics of the Earth and Planetary Interiors*, 187(3):78–91, Aug 2011.

[40] G. Allen Gary. Plasma Beta above a Solar Active Region: Rethinking the Paradigm. *Solar Physics*, 203(1):71–86, Oct 2001.

[41] G. Allen Gary and David Alexander. Constructing the Coronal Magnetic Field By Correlating Parameterized Magnetic Field Lines With Observed Coronal Plasma Structures. *Solar Physics*, 186:123–139, May 1999.

[42] E. Marsch. Solar wind and kinetic heliophysics. *Annales Geophysicae*, 36(6):1607–1630, 2018.

[43] X. H. Sun, W. Reich, A. Waelkens, and T. A. Enßlin. Radio observational constraints on Galactic 3D-emission models. *Astron. Astrophys.* , 477(2):573–592, Jan 2008.

[44] Ronnie Jansson and Glennys R. Farrar. A New Model of the Galactic Magnetic Field. , 757(1):14, Sep 2012.

[45] J. Xu and J. L. Han. Magnetic fields in the solar vicinity and in the Galactic halo. *Mon. Not. R. Astron. Soc.* , 486(3):4275–4289, Jul 2019.

[46] Rainer Beck, Luke Chamandy, Ed Elson, and Eric G. Blackman. Synthesizing observations and theory to understand galactic magnetic fields: Progress and challenges. *Galaxies*, 8(1):4, Dec 2019.

58

[47] David Moss and Dmitry Sokoloff. Magnetic fields around galactic discs. *Galaxies*, 7(1):36, Mar 2019.

[48] V Heesen, M Krause, R Beck, B Adebahr, D J Bomans, E Carretti, M Dumke, G Heald, J Irwin, B S Koribalski, D D Mulcahy, T Westmeier, and R-J Dettmar. Radio haloes in nearby galaxies modelled with 1D cosmic ray transport using spinnaker. *Mon. Not. R. Astron. Soc.* , 476(1):158–183, 01 2018.

[49] K. Ferrière. Plasma turbulence in the interstellar medium. *Plasma Physics and Controlled Fusion*, 62(1):014014, Jan 2020.

[50] Joss Bland-Hawthorn, Ken Freeman, and Francesca Matteucci. The Origin of the Galaxy and Local Group. Saas-Fee Advanced Course, Jan 2014.

[51] Dmitrii Sokoloff and Anvar Shukurov. Regular magnetic fields in coronae of spiral galaxies. , 347(6288):51–53, Sep 1990.

[52] A. Brandenburg, K. J. Donner, D. Moss, A. Shukurov, D. D. Sokolov, and I. Tuominen. Dynamos in discs and halos of galaxies. *Astron. Astrophys.* , 259:453–461, Jun 1992.